

# Evaluation of High Mountain Asia -Land Data Assimilation System Part I: A hyper-resolution terrestrial modeling system

Yuan Xue<sup>1</sup>, Paul Houser<sup>1</sup>, Viviana Maggioni<sup>1</sup>, Yiwen Mei<sup>2</sup>, Sujay Kumar<sup>3</sup>, and Yeosang Yoon<sup>3</sup>

<sup>1</sup>George Mason University

<sup>2</sup>University of Michigan

<sup>3</sup>NASA/GSFC

November 21, 2022

## Abstract

This first paper of the two-part series focuses on demonstrating the predictability of a hyper-resolution, offline terrestrial modeling system used for the High Mountain Asia (HMA) region. To this end, this study systematically evaluates four sets of model simulations at point scale, basin scale, and domain scale obtained from different spatial resolutions including 0.01 degree ( 1-km) and 0.25 degree ( 25-km). The assessment is conducted via comparisons against ground-based observations and satellite-derived reference products. The key variables of interest include surface net shortwave radiation, surface net longwave radiation, skin temperature, near-surface soil temperature, snow depth, snow water equivalent, and total runoff. In the evaluation against ground-based measurements, the superiority of the 0.01 degree estimates are mostly demonstrated across relatively complex terrain. Specifically, hyper-resolution modeling improves the skill in meteorological forcing estimates (except precipitation) by 9% relative to coarse-resolution estimates. The model forced by downscaled forcings in its entirety yields the highest predictability skill in model output states as well as precipitation, which improves the skill obtained by coarse-resolution estimates by 7%. These findings, on one hand, corroborate the importance of employing the hyper-resolution versus coarse-resolution modeling in areas characterized by complex terrain. On the other hand, by evaluating four sets of model simulations forced with different precipitation products, this study emphasizes the importance of accurate hyper-resolution precipitation products to drive model simulations.



## Abstract

This first paper of the two-part series focuses on demonstrating the predictability of a hyper-resolution, offline terrestrial modeling system used for the High Mountain Asia (HMA) region. To this end, this study systematically evaluates four sets of model simulations at point scale, basin scale, and domain scale obtained from different spatial resolutions including  $0.01^\circ$  ( $\sim 1$ -km) and  $0.25^\circ$  ( $\sim 25$ -km). The assessment is conducted via comparisons against ground-based observations and satellite-derived reference products. The key variables of interest include surface net shortwave radiation, surface net longwave radiation, skin temperature, near-surface soil temperature, snow depth, snow water equivalent, and total runoff. In the evaluation against ground-based measurements, the superiority of the  $0.01^\circ$  estimates are mostly demonstrated across relatively complex terrain. Specifically, hyper-resolution modeling improves the skill in meteorological forcing estimates (except precipitation) by 9% relative to coarse-resolution estimates. The model forced by downscaled forcings in its entirety yields the highest predictability skill in model output states as well as precipitation, which improves the skill obtained by coarse-resolution estimates by 7%. These findings, on one hand, corroborate the importance of employing the hyper-resolution versus coarse-resolution modeling in areas characterized by complex terrain. On the other hand, by evaluating four sets of model simulations forced with different precipitation products, this study emphasizes the importance of accurate hyper-resolution precipitation products to drive model simulations.

## 1 Introduction

High Mountain Asia (HMA) forms the headwaters of river systems, e.g., Yangtze, Yellow, Mekong, Brahmaputra, Indus, and Ganges Rivers, that provide fresh water supply for more than a billion people in the region for the purposes of downstream irrigation, hydropower generation, and general consumption (Armstrong et al., 2019). Meteorological and hydrological conditions in such mountainous environment are poorly monitored due to terrain inaccessibility and financial insufficiency (Ghatak et al., 2018). To overcome the limitations imposed by inadequate ground-based stations, previous studies generally utilized global land surface models or regional hydrological models to represent the hydro-meteorological processes involved across the HMA region. For example, Immerzeel, Droogers, De Jong, and Bierkens (2009) evaluated runoff simulations in a Himalayan river basin using the Snowmelt Runoff Model forced by remotely sensed pre-

53 precipitation at a spatial resolution of  $0.25^\circ$ . Yoon et al. (2019) provided a thorough eval-  
54 uation of the terrestrial water budget estimation (i.e., precipitation, evapotranspiration,  
55 runoff, and terrestrial water storage) over HMA using a suite of uncoupled global land  
56 surface models at a spatial resolution of  $0.25^\circ$ . Further, the study conducted by Ghatak  
57 et al. (2018) evaluated the Noah land surface model-derived runoff simulations in a HMA  
58 region at a spatial resolution of 5-km. To our current knowledge, there exists no pub-  
59 lished study performing land surface model simulations finer than 5-km for the entire  
60 HMA for a relatively long period (e.g., more than 10 years).

61 As pointed out by Singh, Reager, Miller, and Famiglietti (2015), increasing com-  
62 putational efficiency and the need for improved accuracy are driving the development  
63 of “hyper-resolution” land surface models that can be implemented at regional scales,  
64 with spatial resolutions of 1-km or even finer. In addition, previous studies emphasized  
65 that high spatial heterogeneity over complex terrain requires land surface model simu-  
66 lations to be implemented at relatively high spatial resolutions (e.g., Zhao and Li (2015)).  
67 In addition to the tremendous amount of computational resources, one of the primary  
68 challenges of land surface modeling at hyper-resolution is the lack of forcing datasets at  
69 such resolution (Kollet et al., 2010; Singh et al., 2015). That is, we simply do not have  
70 reliable regional-scale 1-km in-situ or satellite observational capabilities from which to  
71 derive all meteorological forcing variables required as input into land surface models. Thanks  
72 to the recent developments in physical, and statistical downscaling approaches (e.g., Mei,  
73 Maggioni, Houser, Xue, and Rouf (2020); Rouf, Mei, Maggioni, Houser, and Noonan (2019)),  
74 which allows hyper-resolution forcing fields to be derived from coarser-resolution data  
75 based on ancillary information (e.g., land cover, surface roughness, and topography). Us-  
76 ing Yoon et al. (2019) as a benchmark, in this study, we attempt to address the follow-  
77 ing science question: “to what extent does the development of hyper-resolution forcing  
78 input improve or worsen land surface modeling, compared to ground-based observations  
79 or satellite-derived reference products”? To this end, this study systematically evaluates  
80 the  $0.01^\circ$  ( $\sim 1$ -km) and  $0.25^\circ$  ( $\sim 25$ -km) model simulations at point-scale, basin-scale,  
81 and domain-scale. The key variables of interest include various downscaled meteorolog-  
82 ical forcing input, as well as model output of surface net shortwave radiation, surface net  
83 longwave radiation, skin temperature, near-surface soil temperature, snow depth, snow  
84 water equivalent, and total runoff.

85 The ultimate goal of this research is to evaluate the newly-developed, hyper-resolution  
 86 High Mountain Asia - Land Data Assimilation System (version 1) from 2003 to 2016.  
 87 The High Mountain Asia - Land Data Assimilation System is intended to provide spa-  
 88 tially and temporally continuous land surface estimates, which are believed essential to  
 89 capture the spatio-temporal evolution of hydrometeorological conditions and their as-  
 90 sociated processes across HMA. Part I, presented in this manuscript, focuses on demon-  
 91 strating the predictability of a hyper-resolution (at  $\sim 1$ -km spatial resolution), offline  
 92 (uncoupled to the atmosphere) terrestrial modeling system (without assimilation) used  
 93 for complex terrain regions.

## 94 **2 Data and Methods**

### 95 **2.1 Study domain and models**

96 The study domain is the HMA region bounded between  $20^{\circ}\text{N}$  and  $41^{\circ}\text{N}$  and  $66^{\circ}\text{E}$   
 97 and  $101^{\circ}\text{E}$ . Meteorological fields from the European Centre for Medium-Range Weather  
 98 Forecasts (ECMWF; Molteni, Buizza, Palmer, and Petroliaxis (1996)) and Climate Haz-  
 99 ards Group InfraRed Precipitation with Station data, Version 2 (CHIRPS; Funk et al.  
 100 (2015)) (and two precipitation variants derived from CHIRPS; see Table 1) are used in  
 101 this study. The ECMWF product is originally on a TL511 triangular truncation, linear  
 102 reduced gaussian grid ( $0.25^{\circ}$ ) for four synoptic hours: 00, 06, 12, and 18 UTC. The ECMWF  
 103 forcing fields employed in this study include air temperature, specific humidity, down-  
 104 ward longwave flux, downward shortwave flux, wind speed, and surface pressure. The  
 105 CHIRPS precipitation product has a native spatial resolution of  $0.05^{\circ}$  at a daily time  
 106 scale. Yoon et al. (2019) demonstrated that the joint use of ECMWF and CHIRPS forc-  
 107 ings provides the best model estimates at  $0.25^{\circ}$  spatial resolution for daily output of wa-  
 108 ter balance components.

109 Four sets of model simulations are evaluated in this study, which are summarized  
 110 in Table 1. 1) In “HMA-Coarse” (also denoted as “HMA-CS” in figures), the meteo-  
 111 logical inputs (i.e., air temperature, humidity, surface pressure, wind, downward short-  
 112 wave, and longwave radiation) are adjusted for the elevation differences through lapse-  
 113 rate and slope-aspect correction methods (Kumar, Peters-Lidard, Mocko, & Tian, 2013).  
 114 Inputs obtained from ECMWF and CHIRPS are spatially interpolated and aggregated  
 115 onto the same  $0.25^{\circ}$  grid for generating model output. 2) In “HMA-GMU”, all meteo-

116 meteorological inputs are downscaled using physically-based and statistically-based algorithms  
117 onto the  $0.01^\circ$  grid for model estimates. Section 2.1.1 summarizes key steps used in the  
118 downscaling process. 3) In “HMA-CHIRPS”, model output estimates are at a spatial  
119 resolution of  $0.01^\circ$ . Except for the precipitation field, all other meteorological forcings  
120 remain the same as “HMA-GMU”. The precipitation field is replaced with original CHIRPS,  
121 which is then spatially interpolated onto the same  $0.01^\circ$  grid for model estimates using  
122 the simplistic conservative interpolation scheme. 4) In “HMA-corr-CHIRPS”, model out-  
123 put estimates are at a spatial resolution of  $0.01^\circ$ . Except for precipitation, all other me-  
124 teorological forcings remain the same as “HMA-GMU” and “HMA-CHIRPS”. The pre-  
125 cipitation field is replaced with the bias-corrected CHIRPS (see Section 2.1.2 for details),  
126 which is then spatially interpolated onto the same  $0.01^\circ$  grid for model estimates using  
127 the simplistic conservative interpolation scheme.

128 The land surface model used in this study is the baseline Noah-MP (Niu et al., 2011;  
129 Z.-L. Yang et al., 2011). Noah-MP is enhanced from the original Noah land surface model  
130 through the addition of improved model physics (i.e., dynamic vegetation phenology, a  
131 carbon budget and carbon-based photosynthesis, an explicit vegetation canopy layer, a  
132 multilayer snowpack representation and a groundwater module) and multi-parameterization  
133 options. We used Noah-MP version 3.6 within the NASA Land Information System (LIS)  
134 7.2 version (Kumar et al., 2006). The Noah-MP model configuration options are the same  
135 as Xue et al. (2019), and Yoon et al. (2019), which were shown to provide relatively good  
136 agreement with reference datasets in simulating hydrological conditions. The land sur-  
137 face model simulations are conducted with a 15-min time step for a 14-year time period  
138 (2003–2016) to generate daily output of water balance components. The initial condi-  
139 tions for the runs are generated by appropriate spin-up strategies as described by Xue  
140 et al. (2019) and Yoon et al. (2019), and then reinitializing all model runs in 2003.

### 141 ***2.1.1 Downscaling of meteorological forcings***

142 Following Rouf et al. (2019), meteorological forcings including near-surface ( $\sim 10$   
143 m above the ground) air temperature (denoted as “ $T_a$ ”), surface pressure (denoted as  
144 “ $p_r$ ”), near-surface ( $\sim 10$  m above the ground) specific humidity (denoted as “ $q$ ”), near-  
145 surface ( $\sim 10$  m above the ground) wind speed (denoted as “ $w$ ”), downward surface short-  
146 wave radiation (denoted as “SW”), and downward surface longwave radiation (denoted  
147 as “LW”) obtained from ECMWF are spatially downscaled from their original resolu-

148 tions ( $0.25^\circ$ ) onto the  $0.01^\circ$  model grid. The symbol of “ $\tilde{(\cdot)}$ ” denotes the variable at  $0.01^\circ$   
 149 model grid. The downscaling methods are developed by the George Mason University  
 150 (GMU) research team, and therefore we refer to the downscaled meteorological forcings  
 151 as GMU downscaled forcings. The downscaled air temperature in the unit of K is com-  
 152 puted as Marshall and Plumb (1989):

$$153 \quad \tilde{T}_a = T_a + \Gamma_a(\tilde{Z} - Z), \quad (1)$$

154 where  $Z$  (m) is the Shuttle Radar Topography Mission (SRTM) digital elevation model  
 155 derived elevation at  $0.25^\circ$ ,  $\tilde{Z}$  (m) is the elevation derived at  $0.01^\circ$  (see Figure 1a), and  
 156  $\Gamma_a$  (K/m) is the spatially distributed dynamic lapse rate in air temperature (Rouf et al.,  
 157 2019). The downscaled surface pressure in the unit of Pa is computed as Cosgrove et al.  
 158 (2003):

$$159 \quad \tilde{p}_r = p_r \exp\left(-\frac{g(\tilde{Z} - Z)}{RT_m}\right), \quad (2)$$

160 where  $\exp(\cdot)$  is the exponential operator.  $R$  ( $= 287 \text{ J}/(\text{kg} \cdot \text{K})$ ) is the ideal gas constant,  
 161  $g$  ( $= 9.81 \text{ m}/\text{s}^2$ ) is the gravitational acceleration constant, and  $T_m$  (K) is the mean air  
 162 temperature computed from  $T_a$  and  $\tilde{T}_a$ . The downscaled specific humidity in the unit  
 163 of kg/kg is computed as Lawrence (2005):

$$164 \quad \tilde{q} = \frac{0.622\tilde{E}}{\tilde{p}_r - 0.378\tilde{E}}, \quad (3)$$

165 where

$$166 \quad \tilde{E} = C_1 \exp\left(\frac{C_2\tilde{T}_d}{\tilde{T}_d + C_3}\right), \quad (4)$$

$$167 \quad \tilde{T}_d = T_d + \Gamma_d(\tilde{Z} - Z), \quad (5)$$

168 where for water,  $C_1$  ( $= 611.21 \text{ Pa}$ ),  $C_2$  ( $= 17.268$ ),  $C_3$  ( $= 238.88^\circ\text{C}$ ), and for ice,  $C_1$  ( $=$   
 169  $611.15 \text{ Pa}$ ),  $C_2$  ( $= 22.452$ ),  $C_3$  ( $= 272.55^\circ\text{C}$ ) as noted in Buck (1981).  $T_d$  (K) is the dew  
 170 point temperature, and  $\Gamma_d$  (K/m) is the spatially distributed dynamic lapse rate in dew  
 171 point temperature. The downscaled wind speed in the unit of m/s is computed as Bohn  
 172 and Vivoni (2019); Rouf et al. (2019); Tao and Barros (2018):  
 173

$$174 \quad \tilde{w} = \frac{\tilde{\mu}_*}{\kappa} \ln \frac{H}{\tilde{z}_0}, \quad (6)$$

175 where

$$176 \quad \tilde{\mu}_* = \mu_* \left(\frac{\tilde{z}_0}{z_0}\right)^{0.09}, \quad (7)$$

$$177 \quad \tilde{z}_0 = \tilde{k} \sum_{i=1}^M \tilde{\rho}_i z_{0,i} + z_0 - k \sum_{i=1}^M \rho_i z_{0,i}, \quad (8)$$

178

179 where  $\ln(\cdot)$  is the natural logarithm operator,  $\mu_*$  (m/s) is the friction velocity,  $z_0$  (m)  
 180 is the surface roughness,  $\kappa$  ( $= 0.41$ ) is the Von Kármán constant,  $H$  ( $= 10$  m) is the mea-  
 181 surement height above the ground, and  $M$  is the number of land cover types.  $\rho_i$  is the  
 182 fractional values of the  $i^{th}$  land cover type.  $k$  represents the temporal variability of the  
 183 Moderate Resolution Imaging Spectroradiometer (MODIS) derived normalized differ-  
 184 ence vegetation index (NDVI), which is computed as the ratio of the NDVI obtained from  
 185 the current time step versus the annual mean of the NDVI. The downscaled incident short-  
 186 wave radiation in the unit of  $W/m^2$  is computed as Fiddes and Gruber (2014); Gupta  
 187 and Tarboton (2016); Ruiz-Arias, Alsamamra, Tovar-Pescador, and Pozo-Vázquez (2010);  
 188 Tao and Barros (2018):

$$189 \quad \tilde{S}W = \delta \cos(\theta) \exp(\tau(\tilde{p}_r - p_r)) SW_b + F_v SW_d + \alpha F_t (\tilde{S}W_b + (1 - F_v) \tilde{S}W_d), \quad (9)$$

190 where  $SW_b$  ( $W/m^2$ ) is the direct shortwave radiation, and  $SW_d$  ( $W/m^2$ ) is the diffuse  
 191 shortwave radiation.  $\delta$  is the binary shadowing mask indicating whether the grid cell is  
 192 blocked by the shadow of nearby terrain,  $\cos(\theta)$  is the cosine of the solar illumination  
 193 angle,  $\tau$  ( $Pa^{-1}$ ) is the broadband attenuation coefficient,  $\alpha$  is the MODIS derived sur-  
 194 face albedo,  $F_v$  is the fractional value of the visible sky, and  $F_t$  is the terrain configu-  
 195 ration factor, which is computed as the function of terrain slope and  $F_v$ . The downscaled  
 196 longwave radiation in the unit of  $W/m^2$  is computed as Fiddes and Gruber (2014); Konzelm-  
 197 mann et al. (1994):

$$198 \quad \tilde{L}W = (\tilde{\epsilon}_c + \Delta\epsilon) \sigma \tilde{T}_a^4, \quad (10)$$

199 where

$$200 \quad \tilde{\epsilon}_c = 0.23 + 0.484 \left( \frac{\tilde{E}}{\tilde{T}_a} \right)^{\frac{1}{8}}, \quad (11)$$

$$201 \quad \Delta\epsilon = \frac{LW}{\sigma T_a^4} - \epsilon_c, \quad (12)$$

202 where  $\sigma$  ( $= 5.67 \times 10^{-8} W/(m^2 \cdot K^4)$ ) is the Stefan-Boltzmann constant, and  $\epsilon_c$  is the  
 203 clear-sky emissivity.  
 204

205 The original  $0.05^\circ$ /daily CHIRPS precipitation is spatially and temporally down-  
 206 scaled to  $0.01^\circ$ /6-hourly by weighting factors. To disaggregate CHIRPS to  $0.01^\circ$ , spatially-  
 207 distributed weighting factors are derived from daily cumulative downscaled  $0.01^\circ$  ECMWF  
 208 precipitation, which is derived from the original  $0.25^\circ$ /6-hourly ECMWF precipitation  
 209 following Mei et al. (2020). The kernel of the Mei et al. (2020) precipitation downscal-  
 210 ing framework lies in a random forest (RF) classification along with a regression algo-  
 211 rithm. The framework first applies the recursive feature elimination algorithm to select

important predictors in terms of their predictive values to the daily cumulative ECMWF precipitation from a list of potential predictors. There are 13 potential predictors including eight meteorological variables (air and dew point temperature, surface pressure, specific and relative humidity, longwave and shortwave radiation, and wind speed) and five auxiliary variables (vegetation index with 30-day and 60-day lag, latitude, longitude, and day of year). The meteorological variables are either adopted or derived from the down-scaled  $0.01^\circ$  ECMWF estimates. For each year from 2003 to 2016, the first seven predictors with higher predictive values are selected as important predictors. In a next step, with the identified predictors, RF classification models are trained to a binary precipitation mask defining rainy (i.e., daily cumulative precipitation being greater than 0 mm) and non-rainy grid cells and RF regression models are trained to the daily cumulative precipitation for rainy grid cells (Note: one RF classification and one RF regression model for a year). Then, the trained RF classification models are used to produce the  $0.01^\circ$  daily binary precipitation masks with the  $0.01^\circ$ /daily predictors. Finally, the RF regression models are used to estimate the daily cumulative precipitation for rainy grid cells (inferred by the  $0.01^\circ$  precipitation masks) with the identified predictors.

After attaining the  $0.01^\circ$ /daily ECMWF precipitation, the  $0.05^\circ$ /daily CHIRPS precipitation is spatially disaggregated following the equations below:

$$pd_{\tilde{C}} = \begin{cases} \frac{pd_{\tilde{E},i}}{\frac{1}{N} \sum_{i=1}^N pd_{\tilde{E},i}} pd_C, & \text{if } \frac{1}{N} \sum_{i=1}^N pd_{\tilde{E},i} > 0, \\ pd_C, & \text{if } \frac{1}{N} \sum_{i=1}^N pd_{\tilde{E},i} = 0 \end{cases} \quad (13)$$

where  $pd_E$  and  $pd_C$  represent the daily cumulative precipitation from ECMWF and CHIRPS, respectively.  $N$  is the total number of  $0.01^\circ$  grid cells within a  $0.05^\circ$  grid cell. The term of  $\frac{pd_{\tilde{E},i}}{\frac{1}{N} \sum_{i=1}^N pd_{\tilde{E},i}}$  denotes the spatially distributed weighting factors, which quantifies the  $0.01^\circ$  variability of precipitation within the  $0.05^\circ$  grid cells. In the case that all  $0.01^\circ$  grid cells within a  $0.05^\circ$  grid cell have null precipitation,  $pd_C$  is distributed evenly. The daily cumulative CHIRPS precipitation is then multiplied by a temporal weighting factor to attain the 6-hourly precipitation value at  $0.01^\circ$  (denoted as " $pt_{\tilde{C}}$ "). The temporal weighting factor is derived from the  $0.25^\circ$ /6-hourly ECMWF precipitation, written as:

$$pt_{\tilde{C}} = \begin{cases} \frac{pt_{E,t}}{\sum_{t=1}^T pt_{E,t}} pd_{\tilde{C}}, & \text{if } \sum_{t=1}^T pt_{E,t} > 0, \\ pd_{\tilde{C}}, & \text{if } \sum_{t=1}^T pt_{E,t} = 0 \end{cases} \quad (14)$$

where  $pt_E$  denotes the 6-hourly ECMWF precipitation.  $T$  is the total number of time steps within one day. Similar to Equation 13, the term of  $\frac{pt_{E,t}}{\sum_{t=1}^T pt_{E,t}}$  is the 6-hourly tem-

poral weighting factor used to distribute the daily cumulative precipitation; if all 6-hourly precipitation values are zeros within a day,  $\tilde{p}d_C$  is distributed evenly.

### 2.1.2 Bias-corrected CHIRPS

The bias-corrected CHIRPS are generated using the original CHIRPS at  $0.05^\circ$  multiplied with the monthly, spatially-distributed correction factors given by Beck et al. (2020). Their study used streamflow observations from 9372 stations for calibrations of several state-of-the-art (quasi-) global precipitation climatologies. Monthly climatological bias correction factors were calculated by disaggregating the long-term bias correction factors on the basis of gauge catch efficiencies. An example of the spatially-distributed precipitation correction factors as applied in CHIRPS product in February across HMA can be seen from Figure 1b. The domain-averaged precipitation correction factor is 1.43, with relatively high correction factors presence along Karakoram and Himalayan ranges. As noted in Beck et al. (2020), these regions exhibit marked elevation gradients, sparse gauge networks, and substantial snowfall: all factors that tend to favor precipitation underestimation, and therefore, the newly-generated bias-corrected CHIRPS product is intended to increase the magnitude of precipitation across HMA (see Figure 11).

## 2.2 Ground-based measurements of meteorological conditions

A summary of ground-based measurements of meteorological conditions used for evaluation is listed in Tables 3 and 4. These measurements include air temperature, wind speed, specific humidity, surface pressure, incident shortwave radiation, incident long-wave radiation, and total precipitation. These dataset are obtained from 1) the Chinese Meteorological Administration (CMA), namely the Dataset of Daily Climate Data From Chinese Surface Stations for Global Exchange (V3.0) ([https://data.cma.cn/en/?r=data/detail&dataCode=SURF\\_CLI\\_CHN\\_MUL\\_DAY\\_CES\\_V3.0&keywords=daily](https://data.cma.cn/en/?r=data/detail&dataCode=SURF_CLI_CHN_MUL_DAY_CES_V3.0&keywords=daily)), or 2) the Coordinated Enhanced Observing Period (CEOP) Asia Monsoon project ([https://www.eol.ucar.edu/projects/ceop/dm/insitu/sites/ceop\\_ap/](https://www.eol.ucar.edu/projects/ceop/dm/insitu/sites/ceop_ap/)), or 3) the Department of Hydrology and Meteorology in Nepal (DHM), or 4) the Pakistan Meteorology Department (PMD), or 5) the weather underground (WU; <https://www.wunderground.com>). Locations of the ground-based stations are shown in Figures 3 through 5. The discrepancies between model estimates and measurements resulting from different measurement

272 heights are neglected in this study (Note: some in-situ data source do not provide the  
273 measurement height information).

## 274 **2.3 Ground-based measurements of modeled states**

275 A summary of ground-based measurements of modeled states used for evaluation  
276 is listed in Table 4.

### 277 ***2.3.1 Surface radiation***

278 Surface net shortwave radiation and net longwave radiation, calculated as incoming-  
279 minus-outgoing radiant energy fluxes, are evaluated in this study, respectively. The in-  
280 situ radiation measurements are obtained from CEOP. Radiation fluxes are measured  
281 using CM21 Kipp & Zonen (or 2770 Aandera) sensors at a time step of an hour (or twenty  
282 minutes), and at a height of 1.58 m, 2 m (or 3.1 m) above from the ground surface (de-  
283 pending on the station). Daily-averaged, in-situ fluxes are then computed as the tem-  
284 poral mean of the values collected during the 24-hour period. The measurement discrep-  
285 ancies as a result of different sensor installation heights are neglected in this study.

### 286 ***2.3.2 Skin temperature***

287 Two different sources of skin temperature measurements are obtained. First, in-  
288 situ, daily-averaged surface temperature measurements are obtained from CMA. The daily-  
289 averaged surface temperature values are computed by averaging the four measurements  
290 taken by platinum resistance thermometers at 02:00, 08:00, 14:00, and 20:00. Second,  
291 the in-situ surface temperature measurements are obtained from the CEOP Asia Mon-  
292 soon project. Skin temperature are measured at a time step of an hour. Daily-averaged,  
293 in-situ temperatures are then computed as the temporal mean of the values collected dur-  
294 ing the 24-hour period.

### 295 ***2.3.3 Snow depth***

296 The in-situ, daily-averaged snow depth measurements are obtained from 1) the Global  
297 Summary of the Day (GSOD; [https://data.noaa.gov/dataset/dataset/global-surface](https://data.noaa.gov/dataset/dataset/global-surface-summary-of-the-day-gsod)  
298 [-summary-of-the-day-gsod](https://data.noaa.gov/dataset/dataset/global-surface-summary-of-the-day-gsod)), 2) the Contribution to High Asia Runoff from Ice and Snow

299 (CHARIS) project ([http://himatmap.apps.nsidc.org/hma\\_insitu.html](http://himatmap.apps.nsidc.org/hma_insitu.html)), and 3) the  
300 CEOP Asia Monsoon project.

#### 301 **2.3.4 Near-surface soil temperature**

302 Three different sources of the near-surface (5 cm below the ground) soil temper-  
303 ature measurements are obtained. First, in-situ soil temperature measurements are ob-  
304 tained from the CEOP Asia Monsoon project. Near surface soil temperatures are mea-  
305 sured at a time step of an hour or twenty minutes, and at the depth of 3 cm, 4 cm, and/or  
306 5 cm from the ground surface (depending on the station). Daily-averaged temperature  
307 values are then computed as the temporal mean of the temperatures collected during the  
308 24-hour period as a function of the measured depth. It is assumed that measurements  
309 taken at the depth of 5 cm (i.e., center of the soil layer) can best represent the modeled  
310 top-layer of soil (0 - 10 cm). Therefore, the Inverse Distance Weighting method is ap-  
311 plied to the model estimates to match with the measurement depths of 3 cm and 4 cm,  
312 respectively.

313 Second, daily-averaged near-surface soil temperature measurements from one sta-  
314 tion located at (29.76°N, 94.74°E) are obtained from the Southeastern Tibet Observa-  
315 tion and Research Station for the Alpine Environment (SETORS; [http://en.tpdatabase](http://en.tpdatabase.cn/portal/MetaDataInfo.jsp?MetaDataId=197)  
316 [.cn/portal/MetaDataInfo.jsp?MetaDataId=197](http://en.tpdatabase.cn/portal/MetaDataInfo.jsp?MetaDataId=197)) maintained by the Chinese Academy  
317 of Sciences. At this station, soil temperature at a depth of 4 cm below the ground are  
318 measured using a Campbell 107 sensor. We then interpolate the modeled top-layer of  
319 soil (0 - 10 cm) temperature estimates to 4 cm using Inverse Distance Weighting to match  
320 with the measurement depth.

321 Third, in-situ, daily- and spatially-averaged near-surface soil temperature measure-  
322 ments are obtained from the Central Tibetan Plateau Soil Moisture and Temperature  
323 Monitoring Network (CTP-SMTMN; <http://dam.itpcas.ac.cn/rs/?q=data>) main-  
324 tained by the Institute of Tibetan Plateau Research, Chinese Academy of Science. Near-  
325 surface soil temperature measurements are taken at the soil depth in between 0 and 5  
326 cm. Only the range of the near-surface measurement depth is given in the CTP-SMTMN  
327 document without the exact measurement depth (K. Yang et al., 2013). Therefore, the  
328 modeled top-layer soil temperature is used to approximate the measurement taken at  
329 in-situ sites.

### 2.3.5 Total runoff

Table 2 summarizes the main characteristics of the five gauged basins (see Figure 2) in the study area, including drainage area, data source, and mean elevation computed via averaging all grid cells coincident within the given basin. These ground-based measurements are obtained from 1) the Contribution to High Asia Runoff from Ice and Snow (CHARIS) project, or 2) Department of Hydrology and Meteorology in Nepal, or 3) the Global Runoff Data Centre, 56068 Koblenz, Germany ([https://www.bafg.de/GRDC/EN/01\\_GRDC/grdc\\_node.html](https://www.bafg.de/GRDC/EN/01_GRDC/grdc_node.html)). Basin #1 through Basin #5 are listed and organized by drainage area in ascending order in Table 2. It is important to note that only basins with drainage areas of greater than 625 km<sup>2</sup> are included in this study.

Basin #1 originates in the higher mountains in Nepal, where monsoon precipitation constitutes the major source of discharge water. In this basin, there exists a fairly clear rainfall-runoff relationship. That is, strong commonality with precipitation highs to lows matching up with flow magnitudes tends to occur frequently (Hannah, Kansakar, Gerrard, & Rees, 2005). According to Hannah et al. (2005), the flow regime shape in Basin #1 is Class C with marked August peak runoff. The flow regime magnitude in Basin #1 is Class 2 with intermediate amount of both annual total precipitation and total runoff. Note names of “Class C” and “Class 2” are classification schemes based on Hannah et al. (2005).

Basin #2 is a trans-boundary basin lying north-south in the central Himalayan region. It extends from China in the north, and flows through Nepal. The majority of the glaciated region in Basin #2 are located in Tibet, China. The climate is dominated by the Indian summer monsoon system, with the majority of the precipitation falls between June and September. Total runoff varies throughout the year influenced by both snow (and glacier) melt and precipitation (Dandekhya et al., 2017). Peak flows generally occur in July or August as the peak snow and glacier melt coincide with the monsoon peak (Mishra et al., 2018).

Basin #3 originates in Tajikistan and flows towards Uzbekistan. The highest precipitation is often brought by Westerlies during winter and spring periods, with minimums during summer and early autumn periods (Gafurov et al., 2015). The discharge regime is strongly dominated by snow (and glacier) melt in the area during summer time. The increase of water discharge typically begins in April and peaks around July or Au-

362 gust. The recession of the discharge river flow generally commences in August and con-  
363 tinues until February or March, when it reaches its minimum discharge point (Kulma-  
364 tov, Opp, Groll, & Kulmatova, 2013).

365 Basin #4 is located in Tajikistan, which is mainly fed by melting snow and glaciers.  
366 The region is under the continental climate, characterized by a wide temperature vari-  
367 ation throughout the year, with the coldest temperature generally occurring in January.  
368 Similar to Basin #3, Mid Latitude Westerlies are the dominant climatic influence in the  
369 area. Precipitation decreases from west to east. The majority of the annual precipita-  
370 tion falls between February and May (Grin, Schaller, & Ehlers, 2018), while during the  
371 summer and early autumn seasons precipitation presents a minimum.

372 Basin #5 is located in the North Western part of Myanmar. It is dominated by a  
373 mountainous forested terrain, except for the wide flood plain at its lowest southern part  
374 (Yuan et al., 2017). Rainfall is the major driver for the discharge regime in the area. Dur-  
375 ing the southwest monsoon season, Basin #5 is prone to severe floods, due to the high  
376 precipitation intensities with significant spatial and temporal variations (Yuan et al., 2017).  
377 Riverine floods are very common in Basin #5, and they occur as a result of the intense  
378 precipitation when the monsoon troughs or low pressure waves superimpose on the gen-  
379 eral monsoon pattern (Latt, 2015).

## 380 **2.4 Reference remotely sensed products**

381 A summary of remotely sensed products used for evaluation is listed in Table 5.

### 382 **2.4.1 Skin temperature**

383 Similar to the evaluation strategy described in Xue et al. (2019), the reference satellite-  
384 based surface temperature products utilized here are the MODIS/Terra Land Surface  
385 Temperature Daily L3 Global 1-km Grid (MOD11A1, version 6; Wan, Hook, and Hul-  
386 ley (2015)) and the MODIS/Aqua Land Surface Temperature Daily L3 Global 1-km Grid  
387 (MYD11A1, version 6; Wan et al. (2015)). Given the availability of both nighttime and  
388 daytime land surface maps generated by MOD11A1 and MYD11A1 from 2003 to 2016,  
389 we use the simple arithmetic mean of all four measurements to approximate daily-averaged  
390 values. It is important to note that when daytime MOD11A1, nighttime MOD11A1 as  
391 well as daytime MYD11A1, and nighttime MYD11A1 present simultaneously, we cal-

392 culate the daily-averaged surface temperature value; otherwise, a “no-value” flag is ap-  
393 plied.

#### 394 **2.4.2 Snow water equivalent**

395 The reference satellite-based snow water equivalent (SWE) product utilized here  
396 is the Copernicus Global Land Service (CGLS) SWE product (v1.0.2; [https://land.copernicus](https://land.copernicus.eu/global/products/swe)  
397 [.eu/global/products/swe](https://land.copernicus.eu/global/products/swe)) at a spatial resolution of 5 km (Pulliainen, 2006; Takala et  
398 al., 2011) available from 01 January 2006. The CGLS SWE retrieval algorithm combines  
399 information from satellite-based microwave radiometer and optical spectrometer obser-  
400 vations with ground based weather station snow depth measurements and produces daily  
401 Northern Hemispherical scale SWE estimates. The SWE product covers all land surface  
402 areas between latitudes 35°N and 85°N with the exception of mountainous regions, and  
403 glaciers. Therefore, the CGLS SWE product only covers about 16.3% of the entire HMA  
404 land area.

### 405 **2.5 Evaluation methods**

406 All four experiments listed in Table 1 are integrated forward in time at a time step  
407 of 15 minutes, and the daily-averaged model output are generated. The overlapping pe-  
408 riod from 01 February 2003 to 30 November 2016 are used for evaluation in this study.  
409 It is important to note that stations (or grid cells) with records less than 200 days are  
410 excluded from the evaluation. Evaluations are conducted at three different spatial scales.  
411 The point-scale evaluations are performed via comparisons against the closest colocated  
412 ground-based stations. That is, the performance of air temperature, wind speed, spe-  
413 cific humidity, surface pressure, incident shortwave radiation, incident longwave radia-  
414 tion, total precipitation, surface radiation, skin temperature, snow depth, and near-surface  
415 soil temperatures are evaluated at daily time scales via comparisons against in-situ mea-  
416 surements taken by the closest ground-based stations. Goodness-of-fit statistics (see Sec-  
417 tion 2.5.1) are computed and a scoring system (see Appendix A) is designed to rank the  
418 performance of different sets of estimates. It is always difficult to compare 1-km scale  
419 estimates against in-situ scale stations due to the stations’ representativeness issue. There-  
420 fore, if the relative elevation difference between the 1-km scale grid cell and colocated  
421 station is greater than 50%, we deem that the station is unrepresentative of the large-  
422 scale model estimates, and thus such stations are removed from the evaluation.

423 The basin-scale evaluations are conducted for modeled runoff through comparisons  
 424 against ground-based discharge measurements. That is, this study aggregates daily-averaged  
 425 total runoff output onto monthly averages and then evaluates against ground-based dis-  
 426 charge measurements taken at basin outlets. The main reason for comparing runoff at  
 427 monthly scale, rather than at hourly and daily scales is that no river routing routines  
 428 are employed in this study. For each of the model simulation listed in Table 1, the mod-  
 429 eled basin-scale total runoff is computed by integrating the runoff output at each grid  
 430 cell across each of the drainage basin. The goodness-of-fit statistics plus the Nash–Sutcliffe  
 431 model efficiency coefficient (see Section 2.5.1) are computed to evaluate the modeled runoff  
 432 performance.

433 The domain-scale evaluations are conducted between 1) model estimates and ref-  
 434 erence satellite-based products, as well as between 2) meteorological forcings before and  
 435 after being downscaled. That is, the performance of regional model output of skin tem-  
 436 perature, and SWE are evaluated at daily time scales via comparisons against reference  
 437 remotely-sensed products using the goodness-of-fit statistics. All model output and ref-  
 438 erence products are aggregated onto the same  $0.25^\circ$  grid for this set of evaluation. All  
 439 SWE estimates in June, July, and August are excluded from evaluation due to minimized  
 440 coverage of snow in summertime. In addition, the performance of the downscaled me-  
 441 teorological forcings are evaluated using the normalized mutual information index (Sec-  
 442 tion 2.5.2), which is intended to serve as a proxy for the spatial similarity between the  
 443 multi-year averaged forcing variable before and after being downscaled.

### 444 **2.5.1 Evaluation statistics**

445 Goodness-of-fit statistics used for evaluation include bias, root mean squared er-  
 446 ror (RMSE), unbiased root mean squared error (ubRMSE), and correlation coefficient  
 447 (R). The symbol,  $x_{model}$ , is used to denote estimates obtained from the given model sim-  
 448 ulation. The symbol,  $x_{meas}$ , is used to denote in-situ measurements (or reference satellite-  
 449 based measurements) at either daily or monthly time steps (Note: monthly time step is  
 450 only applicable for runoff assessment). The bias is computed as:

$$451 \text{Bias} = \frac{1}{N_t} \sum_{j=1}^{N_t} (x_{model,j} - x_{meas,j}), \quad (15)$$

452 where  $N_t$  denotes the total sample size. A lower absolute value of bias is deemed bet-  
 453 ter at decreasing the systematic errors. RMSE is computed as:

$$454 \quad RMSE = \sqrt{\frac{1}{N_t} \sum_{j=1}^{N_t} (x_{model,j} - x_{meas,j})^2}. \quad (16)$$

455 A lower RMSE reflects decreased systematic errors and random errors. Further, ubRMSE  
 456 is calculated as:

$$457 \quad ubRMSE = \sqrt{(RMSE)^2 - (Bias)^2}. \quad (17)$$

458 A lower ubRMSE reflects reduced amount of random errors. In addition, R is computed  
 459 as:

$$460 \quad R = \frac{\sum_{j=1}^{N_t} (x_{model,j} - \bar{x}_{model})(x_{meas,j} - \bar{x}_{meas})}{\sqrt{\sum_{j=1}^{N_t} (x_{model,j} - \bar{x}_{model})^2} \sqrt{\sum_{j=1}^{N_t} (x_{meas,j} - \bar{x}_{meas})^2}}, \quad (18)$$

461 where  $\bar{x}_{meas}$  is the time-averaged estimates of the measurements, and  $\bar{x}_{model}$  is the time-  
 462 averaged estimates obtained from model simulations. A higher R demonstrates better  
 463 correlations with the reference. Overall, a relatively low absolute value of bias, or low  
 464 RMSE, or low ubRMSE, or high R is deemed as a higher level of accuracy in the model  
 465 estimates.

466 In addition, we compute the Nash–Sutcliffe model efficiency coefficient (NSE) statis-  
 467 tics (Nash & Sutcliffe, 1970) in the basin-scale runoff evaluation. NSEs are used to em-  
 468 phasize peak values in evaluating simulation fit, which can be a useful indicator to dis-  
 469 tinguish the skills among different experiments for peak runoff predictability. NSEs can  
 470 range from -infinity to 1.0. An NSE of 1.0 corresponds to a perfect match between model  
 471 and observed runoff, whereas an NSE less than 0 occurs when the model simulations are  
 472 not better than solely the mean of the observations.

### 473 ***2.5.2 Spatial similarity assessments for downscaled products***

474 Mutual information – without an upper bound – can be used to quantify the sta-  
 475 tistical information shared between two distributions (Cover & Thomas, 1991; Strehl &  
 476 Ghosh, 2002), provides a sound indication of the shared information between two dataset.  
 477 On top of that, the normalized mutual information (NMI) could be further derived as  
 478 a proxy for spatial similarity, which is the normalization of the mutual information in-  
 479 dex to scale the results between 0 (no correlation) and 1 (perfect correlation). That is,  
 480 the NMI close to zero indicates high dissimilarity between the two distributions, whereas  
 481 the NMI close to one indicates high similarity.

482 Following Strehl and Ghosh (2002), we define the NMI between variable  $\mathbf{X}$  and  $\mathbf{Y}$   
 483 as follows:

$$484 \quad NMI(\mathbf{X}, \mathbf{Y}) = \frac{I(\mathbf{X}; \mathbf{Y})}{\sqrt{H(\mathbf{X})H(\mathbf{Y})}}, \quad (19)$$

485 where  $I(\mathbf{X}; \mathbf{Y})$  denotes the mutual information shared between the two variables, and  
 486  $H(\mathbf{X})$  and  $H(\mathbf{Y})$  are the entropies of the two variables, respectively.  $I(\mathbf{X}; \mathbf{Y})$  can be fur-  
 487 ther written as:

$$488 \quad I(\mathbf{X}; \mathbf{Y}) = H(\mathbf{X}) + H(\mathbf{Y}) - H(\mathbf{X}, \mathbf{Y}), \quad (20)$$

489 where  $H(\mathbf{X}, \mathbf{Y})$  denotes the joint entropy of two distributions.

### 490 3 Results

#### 491 3.1 Point-scale evaluations

492 Figure 3 shows the evaluation of air temperature at both  $0.25^\circ$  and  $0.01^\circ$  against  
 493 five sources of ground-based measurements. Except for the evaluation against DHM air  
 494 temperature, the GMU downscaled  $0.01^\circ$  air temperature generally outperforms the  $0.25^\circ$   
 495 one. The superiority of the  $0.01^\circ$  air temperature is mostly demonstrated in averaged  
 496 bias and averaged RMSE improvements, but less so with respect to ubRMSE and R. For  
 497 example, in the comparison against CEOP air temperature, the mean bias is improved  
 498 by 32% from -4.98 K ( $0.25^\circ$ ) to -3.38 K ( $0.01^\circ$ ), and the mean RMSE is improved by 23%  
 499 from 5.44 K ( $0.25^\circ$ ) to 4.17 K ( $0.01^\circ$ ). However, the mean ubRMSE is degraded slightly  
 500 by 0.9% from 1.91 K ( $0.25^\circ$ ) to 1.93 K ( $0.01^\circ$ ), and the mean R (= 0.96) is the same.  
 501 Figure 3 also shows the evaluation of surface pressure at both  $0.25^\circ$  and  $0.01^\circ$  against  
 502 ground-based CMA measurements. The downscaled  $0.01^\circ$  estimate yields a perfect weighted  
 503 score of 4.00 (see Table 3), which means the  $0.01^\circ$  surface pressure is superior to the  $0.25^\circ$   
 504 estimate with respect to all goodness-of-fit statistics in both accuracy and precision mea-  
 505 sures. These two evaluations together signifies the benefits of detailed adjustment of the  
 506 elevation difference as air temperature and pressure are very sensitive to the change of  
 507 altitude especially across highly elevated regions.

508 Similarly, improvements are seen in the downscaled shortwave and longwave radi-  
 509 ation estimates in the evaluation against ground-based measurements. That is, Figure  
 510 4 shows the evaluation of incident shortwave radiation, and incident longwave radiation  
 511 at both  $0.25^\circ$  and  $0.01^\circ$  against CEOP measurements. In general, the  $0.01^\circ$  downward  
 512 longwave and shortwave radiation estimates are superior to those at  $0.25^\circ$  especially with

513 respect to bias and RMSE. For example, in the comparison against CEOP downward  
 514 shortwave radiation, the mean bias is improved by 30% from 12.32 W/m<sup>2</sup> (0.25°) to 8.61  
 515 W/m<sup>2</sup> (0.01°), and the mean RMSE is improved by 3% from 63.02 W/m<sup>2</sup> (0.25°) to 61.21  
 516 W/m<sup>2</sup> (0.01°). In the comparison against CEOP downward longwave radiation, the mean  
 517 bias is improved by 15% from -36.87 W/m<sup>2</sup> (0.25°) to -31.36 W/m<sup>2</sup> (0.01°), and the mean  
 518 RMSE is improved by 6% from 43.91 W/m<sup>2</sup> (0.25°) to 41.23 W/m<sup>2</sup> (0.01°). In addition,  
 519 the improvement in the downscaled 0.01° specific humidity (relative to 0.25°) is mostly  
 520 demonstrated in the mean bias (see Figure 4). That is, the mean bias is improved by 74%  
 521 from -0.0011 kg/kg (0.25°) to -0.0003 kg/kg (0.01°).

522 Figure 4 further shows the evaluation of wind speed at both 0.25° and 0.01° against  
 523 three sources of ground-based measurements. On average, the range of R is generally higher  
 524 (relative to other meteorological fields) possibly due to the uncertainty in wind speed  
 525 measurements and estimates caused by random or turbulent disturbance, especially over  
 526 the complex terrain. Generally, the 0.01° wind speed estimate slightly degrades the 0.25°  
 527 result. That is, the 0.01° wind speed estimate only outperforms the 0.25° estimate in  
 528 the evaluation against CMA ground-based measurements; the 0.25° wind speed estimate  
 529 demonstrates better skills in the evaluation against WU or CEOP measurements. The  
 530 degradations seen in the 0.01° wind speed estimates may be partly caused by the assump-  
 531 tions of the logarithmic wind profile used in the downscaling procedure (Rouf et al., 2019).

532 Table 3 summarized the weighted scores obtained from 0.01° and 0.25° near-surface  
 533 atmospheric forcings estimates, respectively. It is encouraging to see that the hyper-resolution  
 534 modeling improves the skill in meteorological forcing estimates (exclude precipitation)  
 535 by 9% relative to coarse-resolution results. The hyper-resolution modeling outperforms  
 536 the coarse-resolution meteorological forcing estimates (exclude precipitation) in nine out  
 537 of 12 sets of evaluation sources in terms of estimates accuracy and precision.

538 Figure 5 shows the evaluation of the precipitation field used in all experiments, in-  
 539 cluding HMA-Coarse, HMA-GMU, HMA-CHIRPS, and HMA-corr-CHIRPS. It is not  
 540 surprising to see that the bias-corrected CHIRPS precipitation field used in the HMA-  
 541 corr-CHIRPS experiment yields a much higher positive bias compared to the rest of the  
 542 precipitation estimates. This phenomenon is especially notable in the evaluation against  
 543 CMA ground-based measurements in that the difference between the mean bias of pre-  
 544 cipitation estimates obtained from the HMA-corr-CHIRPS experiment at 0.01° is sta-

545 tistically different (at a significance level of 5%) from those obtained from all other three  
 546 sets of experiments. As a result, the bias-corrected CHIRPS yields the lowest skill in pre-  
 547 cipitation estimate according to Table 4. Beck et al. (2020) argued that the disagreement  
 548 between bias-corrected CHIRPS and gauge observations might be attributed to either  
 549 1) gauge under-catch issues or 2) scale mismatch between the model estimates and the  
 550 gauge observations, which is reasonable. In general, the range of R is high and the mean  
 551 value of R is low across all four sets of precipitation fields. The precipitation estimate  
 552 skill varies more significantly over high elevated regions, whereas in flatter regions, four  
 553 sets of precipitation fields demonstrate comparable skills. Comparatively, HMA-Coarse  
 554 achieves the highest skills over relatively flat regions (i.e., with a mean elevation of less  
 555 than 250 m). That is, the aggregated precipitation field used in the HMA-Coarse exper-  
 556 iment at a spatial resolution of  $0.25^\circ$  yields a perfect score of 4.0 in the evaluation against  
 557 precipitation measurements obtained from one WU station at an elevation of 250.0m.  
 558 In relatively high elevations, the downscaled GMU precipitation at  $0.01^\circ$  yields the high-  
 559 est skill among all, followed by the CHIRPS precipitation at  $0.01^\circ$ .

560 Figure 6 shows the evaluation of net shortwave radiation, and net longwave radi-  
 561 ation generated by all experiments, including HMA-Coarse, HMA-GMU, HMA-CHIRPS,  
 562 and HMA-corr-CHIRPS in the comparison against CEOP measurements. It is encour-  
 563 aging to see that all  $0.01^\circ$  net shortwave radiation estimates (obtained from HMA-GMU  
 564 or HMA-CHIRPS or HMA-corr-CHIRPS) generally outperform the  $0.25^\circ$  estimate ob-  
 565 tained from HMA-Coarse, especially in terms of the mean bias. For example, the mean  
 566 bias is improved from  $38.11 \text{ W/m}^2$  (HMA-Coarse) to  $-1.21 \text{ W/m}^2$  (HMA-GMU). Sim-  
 567 ilarly, it is encouraging to see all  $0.01^\circ$  net longwave radiation estimates outperform the  
 568  $0.25^\circ$  estimate. The superiority of the  $0.01^\circ$  net longwave radiation is mostly demonstrated  
 569 in averaged bias and averaged RMSE improvements, but less so with respect to ubRMSE  
 570 and R. For example, the mean bias is improved by 39% from  $-34.80 \text{ W/m}^2$  (HMA-Coarse)  
 571 to  $-21.38 \text{ W/m}^2$  (HMA-corr-CHIRPS), and the mean RMSE is improved by 13% from  
 572  $47.33 \text{ W/m}^2$  (HMA-Coarse) to  $41.27 \text{ W/m}^2$  (HMA-corr-CHIRPS). However, both of the  
 573 mean R and mean ubRMSE are comparable between HMA-Coarse and HMA-corr-CHIRPS.  
 574 In general, HMA-CHIRPS yields the best performance in net shortwave and net long-  
 575 wave radiation estimates, followed by HMA-GMU.

576 Figure 6 further shows the evaluation of snow depth generated by all experiments  
 577 in the comparison against three sources of ground-based stations. Due to the positive

578 bias seen within the bias-corrected CHIRPS precipitation, it is not surprising to see that  
579 HMA-corr-CHIRPS yields the worst performance due to the relatively high estimate of  
580 the snow depth relative to other experiments. For example, the mean bias is degraded  
581 from -0.05 m in HMA-GMU (or -0.06 m in HMA-CHIRPS) to 0.32 m in HMA-corr-CHIRPS.  
582 The mean RMSE is degraded from 0.33 m in HMA-GMU (or 0.29 m in HMA-CHIRPS)  
583 to 0.56 m in HMA-corr-CHIRPS. Further, the ubRMSE is degraded by 54% from 0.24  
584 m (HMA-GMU) to 0.37 m (HMA-corr-CHIRPS). The ubRMSE is degraded by 60% from  
585 0.23 m (HMA-CHIRPS) to 0.37 m (HMA-corr-CHIRPS). Again, it is difficult to discern  
586 whether such bad performance seen in HMA-corr-CHIRPS is due to the erroneous model  
587 estimate itself or under-representative and erroneous ground-based measurements or both.  
588 Based on the sum of the weighted scores, HMA-GMU yields the highest skill in snow depth  
589 estimates, followed by HMA-CHIRPS.

590 Figure 6 also shows the evaluation of skin temperature generated by all experiments  
591 in the comparison against two sources of ground-based stations. It is encouraging to see  
592 that all experiments yield relatively good agreement with the ground-based measurements  
593 in terms of R, with all Rs being greater than 0.9. All  $0.01^\circ$  estimates tend to correct the  
594 positive bias in the  $0.25^\circ$  skin temperature likely arising from the positive bias in the net  
595 shortwave radiation. That is, in the evaluation against CMA skin temperature measure-  
596 ments, the bias decreases from 1.16 K (HMA-Coarse) to 0.03 K (HMA-GMU), and to  
597 0.0009 K (HMA-CHIRPS), and to -0.17 K (HMA-corr-CHIRPS). In the evaluation against  
598 CEOP skin temperature measurements, the bias drops from 1.13 K (HMA-Coarse) to  
599 -1.04 K (HMA-GMU), and to -1.06 K (HMA-CHIRPS), and to -1.47 K (HMA-corr-CHIRPS).  
600 HMA-corr-CHIRPS seems to over-correct the  $0.25^\circ$  skin temperature possibly due to the  
601 over-corrected precipitation, which yields the worst performance among all experiments.  
602 Although HMA-Coarse yields relatively high magnitude of the mean bias relative to both  
603 HMA-GMU and HMA-CHIRPS, HMA-Coarse yields the best performance among all  
604 experiments according to Table 4 mainly due to its superiority in the relatively low val-  
605 ues of interquartile range (IQR; see Appendix A) achieved across all goodness-of-fit statis-  
606 tics.

607 Figure 7 shows the evaluation of soil temperature at different depths generated by  
608 all experiments in the comparison against five sets of ground-based stations. Due to the  
609 difficulty in in-situ soil temperature measurements as well as discrepancies in the mea-  
610 surement and model estimate depth in soil, it is not surprising to see that different ex-

611 periments are superior with respect to different set of ground-based measurements. In  
612 the evaluation against CTP-SMTMN soil temperature measurements, HMA-Coarse out-  
613 performs all  $0.01^\circ$  estimates with respect to all goodness-of-fit statistics. Although there  
614 are 63 CTP-SMTMN stations used for evaluation, only 12 model grid cells at a spatial  
615 resolution of  $0.25^\circ$  are used due to the close proximity of the ground-based stations. That  
616 is, because multiple stations are colocated within one  $0.25^\circ$  grid cell, we evaluate the same  
617 set of  $0.25^\circ$  model estimates against different in-situ measurements colocated within the  
618 model grid cell. Under such circumstances, HMA-Coarse still yields the best performance  
619 partly due to relatively low spatial variability in soil temperature measurements. For ex-  
620 ample, for three  $0.25^\circ$  model grid cells, all with more than five colocated ground-based  
621 stations, the temporally-averaged standard deviations of the ground-based measurements  
622 are 1.28 K, 0.97 K, and 0.96 K. Further, in the evaluation against CEOP 3-cm soil tem-  
623 perature measurements, HMA-corr-CHIRPS yields the best skill, whereas HMA-Coarse  
624 yields the worst performance mainly due to the relatively high positive bias. That is, the  
625 bias of the 3-cm soil temperature estimates in HMA-Coarse, HMA-GMU, HMA-CHIRPS,  
626 and HMA-corr-CHIRPS, are 3.05 K, 0.35 K, 0.36 K, and -0.24 K. In the evaluation against  
627 CEOP 4-cm soil temperature measurements, HMA-Coarse yields the best performance.  
628 HMA-Coarse is superior to all  $0.01^\circ$  estimates mainly in terms of significantly reduced  
629 bias and reduced RMSE. The degradation in the  $0.01^\circ$  estimates relative to  $0.25^\circ$  esti-  
630 mate might be caused by 1) errors in in-situ soil temperature measurements, or 2) over-  
631 correction in the downscaled incident shortwave radiation and net shortwave radiation  
632 although the point-scale evaluation shows better performance in  $0.01^\circ$  estimates (see Fig-  
633 ure 6). It is also possible that the relatively simple Inverse Distance Weighting method  
634 used to apply with the modeled soil temperature estimates to match with the measure-  
635 ment depth may not be appropriate in this case because the temperature gradient may  
636 not be linear. Further, in the evaluation against SETORS 4-cm soil temperature mea-  
637 surements, HMA-GMU yields a close-to-perfect score with improved performance seen  
638 across all goodness-of-fit statistics in terms of the accuracy measure. Compared with the  
639 estimates obtained from HMA-Coarse, HMA-GMU improves the bias by 54% from -9.21  
640 K to -4.21 K. The RMSE is improved by 51% from 9.44 K to 4.61 K, the ubRMSE is  
641 improved by 9% from 2.07 K to 1.88 K, and the R is improved by 6% from 0.94 to 0.95.  
642 Finally, the evaluation against CEOP 5-cm soil temperature measurements shows that  
643 HMA-CHIRPS is slightly superior to other experiments. HMA-CHIRPS' better perfor-

644 mance is largely attributed to its relatively low ranges of IQRs achieved across all goodness-  
 645 of-fit statistics. To summarize, HMA-CHIRPS yields the best performance in soil tem-  
 646 perature estimates, followed by HMA-GMU.

647 Table 4 summarizes the weighted score achieved by each of the experiment with  
 648 respect to each set of the evaluation source. It is found that HMA-GMU yields the high-  
 649 est predictability skill in precipitation and model output states, followed by HMA-CHIRPS.  
 650 Compared with HMA-Coarse, HMA-GMU improves the skill by 7%. However, HMA-  
 651 corr-CHIRPS yields the lowest skill, which degrades HMA-Coarse predictability by 10%.  
 652 These analysis, on one hand, further corroborate the importance of employing the hyper-  
 653 resolution modeling versus coarse-resolution modeling strategy across the complex ter-  
 654 rain; on the other hand, emphasize the importance of the accuracy of the hyper-resolution  
 655 precipitation product used to drive model simulations.

### 656 3.2 Basin-scale evaluations

657 Figure 8 shows the total runoff time series obtained from all experiments for the  
 658 five gauged basins in the evaluation against ground-based measurements. In general, all  
 659 experiments yield relatively good agreement with the ground-based measurements in terms  
 660 of both low flow and high flow seasons, except for Basin #4. In Basin #4, HMA-Coarse  
 661 yields the lowest R of 0.07, and HMA-corr-CHIRPS yields the highest R of 0.66. In ad-  
 662 dition, all experiments yield positive NSEs except for Basin #3 and Basin #4. That is,  
 663 HMA-corr-CHIRPS is the only experiment with a positive NSE of 0.32 for Basin #3.  
 664 In Basin #4, although HMA-CHIRPS achieves the highest NSE of -0.62 among all ex-  
 665 periments, a negative NSE is still not desirable. There can be several reasons contribut-  
 666 ing to the relative poor performance of the modeled runoff simulations in Basin #3 and  
 667 Basin #4. For example, in addition to the shortcoming of neglecting water travel time  
 668 (residence time) within the basin, this study does not model human-related impacts (e.g.,  
 669 water engineering works) and agriculture related activities (e.g., irrigation) in the total  
 670 runoff simulation. Further, the discharge regime is strongly dominated by snow and glacier  
 671 melt within these two basins during summer time (see Section 2.3.5), and therefore, it  
 672 is possible that modeled snow melt discharge enter the stream network too soon due to  
 673 too early onset of snow melt. Therefore, in Part 2 of the future study, we will determine  
 674 if a simple snow cover assimilation scheme can help with modifying the snow melt tim-

675 ing and further improving the runoff modeling performance in snow and glacier dom-  
 676 inated basins.

677 Figure 9 shows all statistics computed for evaluating the performance of HMA-Coarse,  
 678 HMA-GMU, HMA-CHIRPS, and HMA-corr-CHIRPS in comparisons against ground-  
 679 based measurements. In terms of the NSE, model runs for Basin #2, Basin #3, and Basin  
 680 #4 yield relatively low values (all below 0.6) as compared with Basin #1 and Basin #5.  
 681 According to Table 2, Basins #2 through #4 have mean elevations of greater than 3000  
 682 m, whereas Basin #1 has a mean elevation of 1638 m and Basin #5 has a mean eleva-  
 683 tion of 681 m. Therefore, it is likely because precipitation estimates used to force mod-  
 684 els vary more significantly over high elevated regions relative to flatter regions, which is  
 685 also seen in the point-scale precipitation evaluation. In addition, in flatter regions (i.e.,  
 686 Basin #5), all experiments yield relatively high Rs, which are greater than 0.96. Com-  
 687 paratively, HMA-Coarse yields the best performance across all evaluated statistics, and  
 688 HMA-corr-CHIRPS yields the worst performance. In relatively high elevated regions (i.e.,  
 689 Basin #1 through Basin #4),  $0.01^\circ$  runoff estimates obtained from HMA-GMU, HMA-  
 690 CHIRPS, or HMA-corr-CHIRPS are generally superior to  $0.25^\circ$  runoff estimates obtained  
 691 from HMA-Coarse. In Basin #1, HMA-corr-CHIRPS yields the lowest bias ( $= 2.4 \text{ m}^3/\text{s}$ ),  
 692 lowest RMSE ( $= 14.5 \text{ m}^3/\text{s}$ ), and highest NSE ( $= 0.85$ ), whereas HMA-Coarse yields the  
 693 worst performance across all statistics. In Basin #2, HMA-corr-CHIRPS seems to over-  
 694 correct the total runoff especially in years 2007 through 2012. As a result, HMA-GMU  
 695 yields the best performance in total runoff in terms of the lowest RMSE ( $= 140.2 \text{ m}^3/\text{s}$ ),  
 696 lowest ubRMSE ( $= 121.5 \text{ m}^3/\text{s}$ ), and highest NSE ( $= 0.53$ ), whereas HMA-Coarse yields  
 697 the worst performance across all statistics. In Basin #3, HMA-corr-CHIRPS significantly  
 698 outperforms other experiments, with a much lower bias ( $= -12.8 \text{ m}^3/\text{s}$ ), lower RMSE ( $=$   
 699  $352.2 \text{ m}^3/\text{s}$ ), higher R ( $= 0.84$ ), and higher NSE ( $= 0.32$ ). The good performance in HMA-  
 700 corr-CHIRPS derived runoff might be attributed to the relatively high correction fac-  
 701 tors as applied to the region (see Figure 1b). In Basin #4, HMA-CHIRPS yields the best  
 702 performance in terms of the lowest absolute value of bias ( $= -81.75 \text{ m}^3/\text{s}$ ), lowest RMSE  
 703 ( $= 194.9 \text{ m}^3/\text{s}$ ), lowest ubRMSE ( $= 177.7 \text{ m}^3/\text{s}$ ), and less negative value of NSE ( $= -$   
 704  $0.62$ ). The over-correction issue in HMA-corr-CHIRPS runoff can also be seen from 2005  
 705 to 2012.

706 Since the bias-corrected CHIRPS precipitation field is obtained through calibrat-  
 707 ing against ground-based runoff measurements, it is probable that ground-based runoff

708 measurements used in the evaluation here are also used to calibrate the bias-corrected  
 709 precipitation product. This argument might be also used to explain why HMA-corr-CHIRPS  
 710 can significantly outperform all other experiments in Basin #1 and Basin #3 especially  
 711 in bias. However, the over-correction issue in the bias-corrected CHIRPS field should not  
 712 be neglected in Basin #2 and Basin #4. Therefore, in Part 2 of the future study, we will  
 713 determine if a snow cover assimilation scheme can help HMA-corr-CHIRPS to mitigate  
 714 much of the positive bias possibly caused by overly-corrected precipitation.

### 715 **3.3 Domain-scale evaluations**

#### 716 *3.3.1 Evaluation of meteorological forcings*

717 Figure 10 summarizes the multi-year averaged daily air temperature, specific hu-  
 718 midity, surface pressure, wind speed, incident shortwave radiation, incident longwave ra-  
 719 diation, and total precipitation before and after being downscaled from 2003 to 2016.  
 720 In general,  $0.01^\circ$  downscaled forcings preserve the spatially and temporally averaged val-  
 721 ues obtained from original  $0.25^\circ$  (or  $0.05^\circ$ ) estimates relatively well. Based on Table 6,  
 722 the computed NMIs between before and after downscaled meteorological forcing field range  
 723 from 0.82 to 0.96, which indicate relatively high similarities shared between the two set  
 724 of forcing fields. The lowest NMI of 0.82 is obtained from the incident shortwave radi-  
 725 ation field evaluation, which is likely due to the introduction of multiple correction fac-  
 726 tors (i.e., clearness index, local illumination, cast-shadowing, sky obstruction, and to-  
 727 pographic configuration; Rouf et al. (2019)) in the shortwave radiation downscaling pro-  
 728 cedure.

729 Figure 11 shows the spatial distribution of the annual mean total precipitation ob-  
 730 tained from HMA-Coarse, HMA-GMU, HMA-CHIRPS, and HMA-corr-CHIRPS. The  
 731 spatially-averaged annual mean precipitation difference between HMA-Coarse and HMA-  
 732 CHIRPS is  $-5.89$  mm/yr, which is largely attributed to the spatial aggregation proce-  
 733 dure in the precipitation field used in the  $0.25^\circ$  estimate. Although the spatially-averaged  
 734 annual mean precipitation difference between HMA-GMU and HMA-CHIRPS is neg-  
 735 ligible ( $= -0.74$  mm/yr), precipitation magnitudes still vary grid-by-grid between these  
 736 two experiments. HMA-corr-CHIRPS yields the highest precipitation magnitude in terms  
 737 of the spatially-averaged mean. For example, compared with the precipitation field used  
 738 in HMA-CHIRPS, the bias-corrected CHIRPS increases the spatially-averaged annual

739 mean precipitation by 23%, with the majority of the notable increases in the mountain-  
740 ous regions. Despite of the discrepancies in magnitudes among all experiments, it is en-  
741 couraging to see that all four total precipitation field reveal similar patterns across HMA.  
742 For example, precipitation intensity exhibits a strong north-south gradient due to oro-  
743 graphic effects. Specifically, along the south slope of the Himalayas, annual precipita-  
744 tion is relatively high due to the prevalence of the Indian monsoon. While the height and  
745 extent of the Himalayas impose a significant barrier to atmospheric circulation patterns  
746 and the northward push of water vapor is greatly limited by the Himalayan mountain  
747 chain, regions north of the orographic barriers (e.g., Tibetan Plateau) receive little pre-  
748 cipitation throughout the year (Bookhagen & Burbank, 2010). Within the Tibetan Plateau  
749 region, there exists a gradual decrease of the annual precipitation from Southeastern Ti-  
750 betan Plateau to Northwestern Tibetan Plateau. The relatively dry Northwestern Ti-  
751 betan Plateau is dominated by the westerlies for almost the entire year as the center of  
752 the mean moisture contribution is concentrated toward the northwest, while the South-  
753 eastern Tibetan Plateau precipitation is more influenced by the summer monsoons as  
754 the center moves more toward the southeast (You, Min, Zhang, Pepin, & Kang, 2015;  
755 Zhang et al., 2019). Overall, generally wetter regions in Bangladesh, eastern India, and  
756 the central and eastern Ganges plains are observed in all three products assessed in this  
757 study, which is consistent with the findings from Bookhagen and Burbank (2010) and  
758 Yoon et al. (2019) using other different precipitation products.

### 759 ***3.3.2 Evaluation of model estimates against satellite-based products***

760 Figure 12 shows the goodness-of-fit statistics computed for HMA-Coarse, HMA-  
761 GMU, HMA-CHIRPS, and HMA-corr-CHIRPS in the evaluation against the CGLS SWE  
762 product from 2006 to 2016 across part of HMA above latitude 35°. It is expected that  
763 the worst agreement (i.e., relatively high magnitudes of bias, RMSE, ubRMSE, and low  
764 R) of all four experiments are colocated with relatively high elevated regions inside the  
765 Tibetan Plateau, to the south of the Kunlun Mountain relative to the north of the Moun-  
766 tain (a.k.a., Taklamakan dessert) due to the difference in different climate regions. Al-  
767 though HMA-corr-CHIRPS yields the best performance in terms of the spatially-averaged  
768 bias (= -1.23 mm) compared with the rest of the experiments due to the higher total pre-  
769 cipitation magnitude, it still yields the worst performance in terms of RMSE (= 9.87 mm)  
770 and ubRMSE (= 9.41 mm). Among HMA-Coarse, HMA-GMU, and HMA-CHIRPS, the

771 two  $0.01^\circ$  SWE estimates obtained from HMA-GMU, and HMA-CHIRPS generally out-  
772 perform the  $0.25^\circ$  SWE estimates obtained from HMA-Coarse across all goodness-of-fit  
773 statistics. In terms of the spatially-averaged bias, both HMA-GMU and HMA-CHIRPS  
774 yield slight improvements relative to HMA-Coarse. The spatially-averaged bias is im-  
775 proved by 13% from -2.29 mm (HMA-Coarse) to -1.99 mm (HMA-GMU), and it is im-  
776 proved by 12% from -2.29 mm (HMA-Coarse) to -2.02 mm (HMA-CHIRPS). Similarly,  
777 the spatially-averaged R derived by HMA-GMU and HMA-CHIRPS are improved slightly  
778 relative to HMA-Coarse. In addition, both HMA-GMU and HMA-CHIRPS yield slight  
779 improvements in RMSE and ubRMSE relative to HMA-Coarse. Overall, HMA-GMU yields  
780 the best performance in SWE estimates in the evaluation against the CGLS SWE prod-  
781 uct, followed by HMA-CHIRPS. This finding also corroborates the results in the ground-  
782 based snow depth evaluation that HMA-GMU achieves the highest score in the snow es-  
783 timates.

784 Figure 13 shows the goodness-of-fit statistics computed for HMA-Coarse, HMA-  
785 GMU, HMA-CHIRPS, and HMA-corr-CHIRPS in the evaluation against the MODIS  
786 skin temperature product from 2003 to 2016 across HMA. The worst agreement (i.e., rel-  
787 atively high magnitudes of bias, RMSE, ubRMSE, and low R) of all four experiments  
788 are along the Himalayas. The spatially-averaged bias is negative for all four experiments,  
789 however, with noticeable positive biases present in Pakistan and Northern India along  
790 Ganges and Indus rivers, covered with cropland. As discussed in Xue et al. (2019), such  
791 positive biases are possibly attributed to the lack of irrigation related activities in the  
792 Noah-MP model, and therefore yield an overestimation of the surface temperature in this  
793 region across all experiments. Comparatively, HMA-Coarse yields the most agreement  
794 (i.e., relatively low magnitudes of bias, RMSE, and ubRMSE) with the MODIS skin tem-  
795 perature product among all experiments, whereas HMA-corr-CHIRPS yields the worst  
796 agreement, which is consistent with the finding obtained from ground-based skin tem-  
797 perature evaluation. Compared with HMA-Coarse, HMA-GMU and HMA-CHIRPS de-  
798 crease the spatially and temporally averaged skin temperature by 1.10 K (from 285.30  
799 K to 284.20 K) and 1.13 K (from 285.30 K to 284.17 K), respectively (not shown). This  
800 reduction in the skin temperature magnitude is mainly caused by the reduction in the  
801 incident shortwave radiation before and after being downscaled (see Figure 10). Since  
802 HMA-Coarse already yields a negative bias in the skin temperature in the evaluation,  
803 the reduction in the HMA-GMU or HMA-CHIRPS derived skin temperature magnitude

804 further exacerbates the negative bias, which leads to significant degradations in terms  
805 of both bias and RMSE. HMA-corr-CHIRPS skin temperature yields more negative bias  
806 than HMA-GMU and HMA-CHIRPS because more precipitation is associated with more  
807 chances of evapotranspiration, which will lead to further reduction in the skin temper-  
808 ature estimates. In Part 2 of the future study, we will determine if a freeze/thaw assim-  
809 ilation scheme can help improving the performance of the  $0.01^\circ$  skin temperature esti-  
810 mates.

#### 811 **4 Conclusions and discussions**

812 This first article of a two-part series focuses on demonstrating the predictability  
813 of a hyper-resolution, offline terrestrial modeling system used for High Mountain Asia  
814 (HMA) region. To this end, this study systematically evaluates four sets of model sim-  
815 ulations obtained from different spatial resolutions including  $0.01^\circ$  ( $\sim 1$ -km) and  $0.25^\circ$   
816 ( $\sim 25$ -km) at point-scale, basin-scale, and domain-scale. The advantages of employing  
817 a hyper-resolution modeling unit (versus the coarse-resolution modeling unit) within the  
818 Noah-MP model are demonstrated in this study, especially in terms of its ability in re-  
819 ducing systematic errors in model estimates. That is, over relatively complex terrain,  
820 the  $0.01^\circ$  modeling demonstrates superiority in estimating air temperature, surface pres-  
821 sure, incident shortwave radiation, incident longwave radiation, specific humidity, pre-  
822 cipitation, surface net shortwave radiation, surface net longwave radiation, snow depth,  
823 and total runoff based on point-scale and basin-scale evaluations. In terms of wind speed,  
824 skin temperature, and near-surface soil temperature, mixed performance – sometimes  
825 improvements and sometimes degradations – are seen in  $0.01^\circ$  estimates relative to  $0.25^\circ$   
826 estimates. The exact reason of the mixed performance seen in  $0.01^\circ$  estimates remains  
827 unclear, but may be partly attributed to measurement errors arising from scale mismatch  
828 or measurement height discrepancies.

829 In the domain-scale evaluations against satellite-based products, HMA-GMU yields  
830 the largest agreement with the CGLS SWE product, and HMA-Coarse yields the largest  
831 agreement with the MODIS skin temperature product. We are aware that skill metrics  
832 computed during these comparisons are impacted by errors in the reference products.  
833 For example, the CGLS SWE product may yield higher uncertainty in estimating rel-  
834 atively deep snow especially over the forested regions. The accuracy of the MODIS skin  
835 temperature product is largely impacted by atmospheric attenuation effect, surface emis-

836 sivity variability, as well as the procedure to derive the daily-averaged value. In this  
837 regard, systematic errors metrics such as bias and RMSE, may be secondary or tertiary  
838 as compared with the random errors measures such as ubRMSE. In Part II of this study,  
839 we will present the effects of the joint assimilation of satellite-based snow cover and freeze/thaw  
840 observations into the system. We will present to what extent the assimilation procedure  
841 will improve or degrade the performance of the  $0.01^\circ$  estimate without assimilation, es-  
842 pecially for the random error measure metrics, such as ubRMSE. It is also hopeful that  
843 some of the over-correction issues seen in HMA-corr-CHIRPS can be reduced by the as-  
844 similation procedure.

845 Among all meteorological forcings used to drive land surface model simulations,  
846 precipitation is undoubtedly one of the most important fields. Through evaluating four  
847 sets of model simulations forced by different precipitation products, it is seen that the  
848  $0.01^\circ$  estimate forced by an inaccurate precipitation representation would lead to mod-  
849 est degradations in model estimates relative to the  $0.25^\circ$  estimate. Among all  $0.01^\circ$  es-  
850 timates, in general, HMA-GMU and HMA-CHIRPS yield relatively high skills in model  
851 estimates. Key conclusions drawn from this study are summarized below:

852 1) In the evaluation against ground-based measurements of air temperature, sur-  
853 face pressure, wind speed, incident shortwave radiation, incident longwave radiation, and  
854 specific humidity, it is found that the hyper-resolution modeling improves the skill in me-  
855 teorological forcing estimates (exclude precipitation) by 9% relative to coarse-resolution  
856 estimates using the sum of the weighted scores as the criteria (see Table 3). The hyper-  
857 resolution modeling outperforms the coarse-resolution meteorological forcing estimates  
858 (exclude precipitation) in 9 out of 12 sets of evaluation sources in terms of estimates ac-  
859 curacy and precision. In terms of precipitation, the downscaled GMU precipitation yields  
860 the highest skill across relatively high elevated regions, which improves the predictabil-  
861 ity skill by 3% relative to the  $0.25^\circ$  aggregated precipitation across the complex terrain.

862 2) In the evaluation against ground-based net shortwave radiation measurements,  
863 all  $0.01^\circ$  estimates generally outperform the  $0.25^\circ$  estimate obtained from HMA-Coarse,  
864 especially in terms of bias and RMSE. Compared with HMA-Coarse performance in net  
865 radiation estimates, HMA-CHIRPS improves the skill by 10%.

866 3) In the evaluation against ground-based snow depth measurements, HMA-GMU  
867 yields the highest skill in snow depth estimates, followed by HMA-CHIRPS. Compared

868 with HMA-Coarse performance in snow depth estimates, HMA-GMU improves the skill  
869 significantly by 39%.

870 4) In the evaluation against ground-based skin temperature measurements, although  
871 HMA-Coarse yields relatively high magnitude of the mean bias relative to both HMA-  
872 GMU and HMA-CHIRPS, HMA-Coarse yields the best performance among all exper-  
873 iments mainly due to its superiority in the relatively low ranges of IQRs achieved across  
874 all goodness-of-fit statistics. Overall, HMA-CHIRPS degrades HMA-Coarse skill in skin  
875 temperature estimates slightly by 6%.

876 5) In the evaluation against ground-based near-surface soil temperature measure-  
877 ments, different experiments demonstrate their superiority with respect to different set  
878 of ground-based measurements. In general, compared with HMA-Coarse performance  
879 in soil temperature estimates, HMA-CHIRPS improves the skill slightly by 6%.

880 6) In the evaluation against ground-based total runoff measurements obtained from  
881 five gauged basins, HMA-Coarse yields the best performance across all evaluated statis-  
882 tics in relatively flat regions. In relatively high elevated regions,  $0.01^\circ$  runoff estimates  
883 obtained from HMA-GMU, HMA-CHIRPS, and HMA-corr-CHIRPS are generally su-  
884 perior to  $0.25^\circ$  runoff estimates obtained from HMA-Coarse.

885 7)  $0.01^\circ$  downscaled forcings preserve the spatially and temporally averaged val-  
886 ues obtained from original  $0.25^\circ$  (or  $0.05^\circ$ ) estimates relatively well with relatively high  
887 spatial similarity.

888 8) In the evaluation against the CGLS SWE product, HMA-GMU yields the most  
889 agreement, followed by HMA-CHIRPS.

890 9) In the evaluation against the MODIS skin temperature product, HMA-Coarse  
891 yields the most agreement.

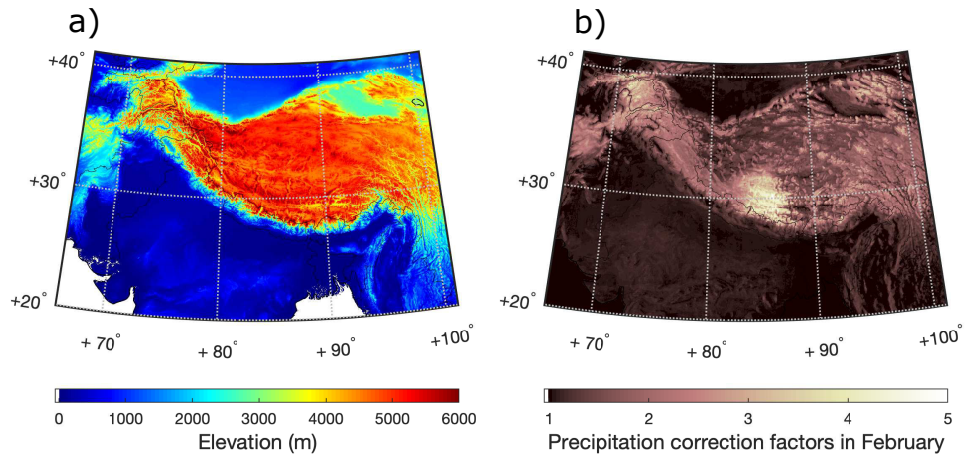


**Figure 1.** a) The SRTM derived HMA elevation map at a spatial resolution of  $0.01^\circ$ . b) An example of the spatially-distributed precipitation correction factors at a spatial resolution of  $0.05^\circ$  as applied in the bias-corrected CHIRPS product in February across HMA.

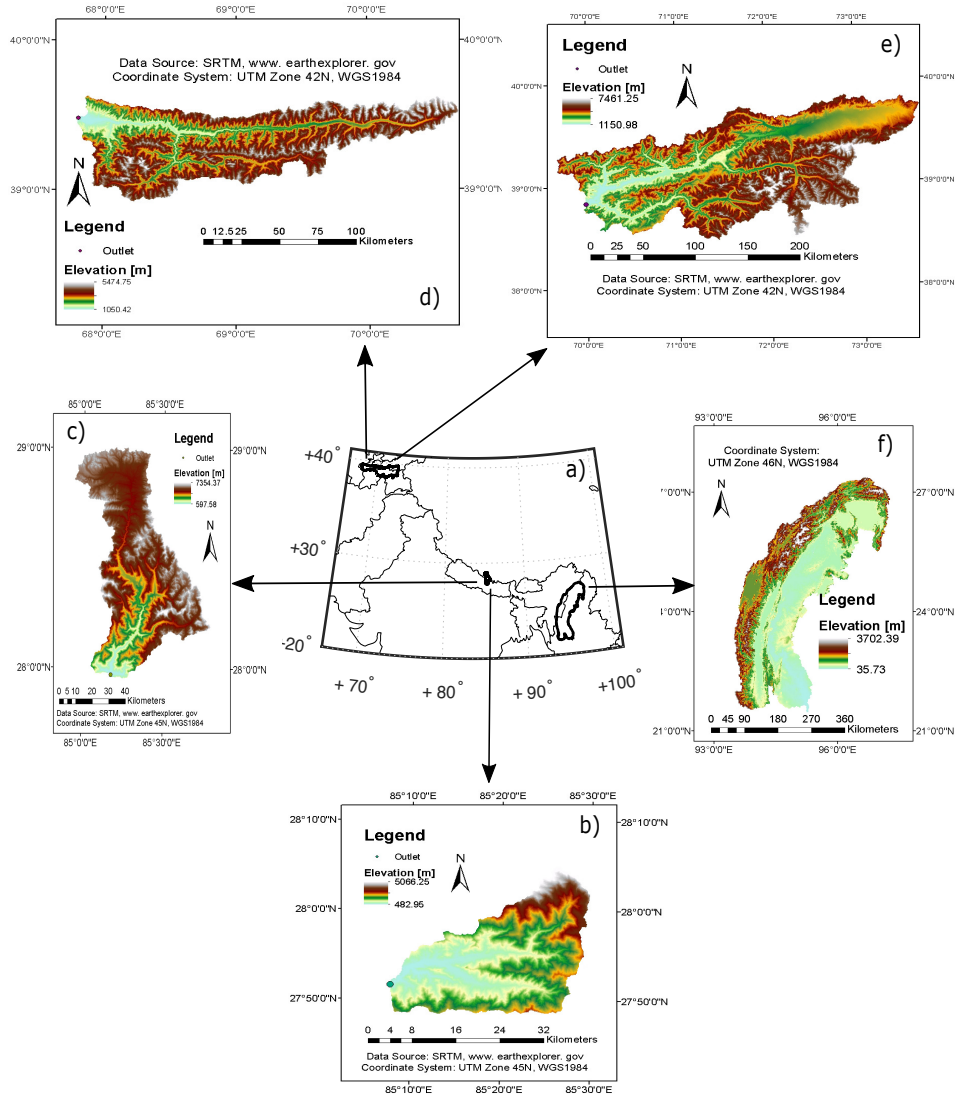


**Figure 2.** a) HMA study domain with gauged basin outlines in black. Gauged Basin #1 through Basin #5 are shown in b) through f) with elevation information and basin outlet locations.

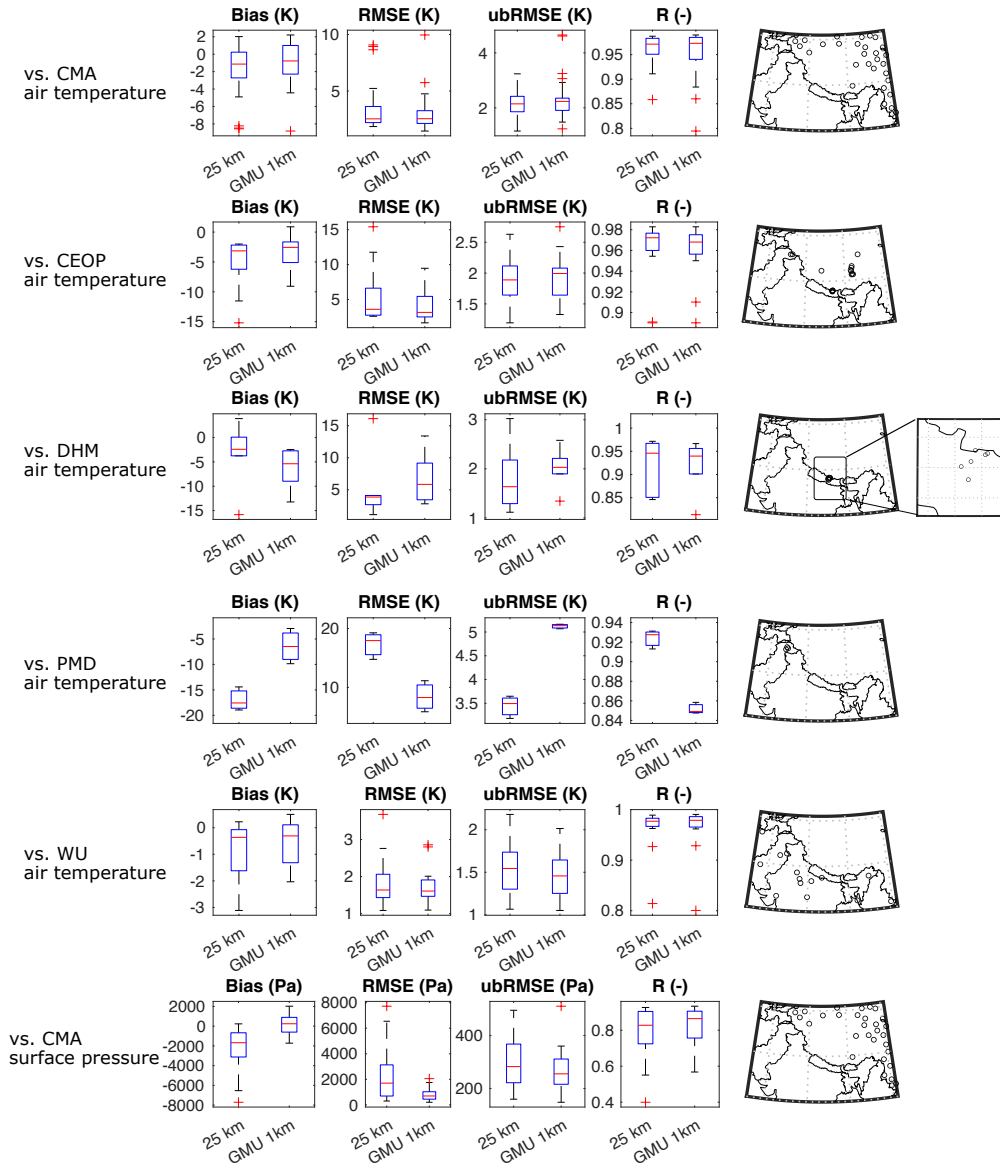


**Figure 3.** Box plots of bias (column 1), RMSE (column 2), ubRMSE (column 3), R (column 4) computed from  $0.25^\circ$  ( $\sim 25$ -km) and downscaled GMU  $0.01^\circ$  ( $\sim 1$ -km) meteorological forcings in the evaluation against ground-based CMA air temperature (row 1), CEOP air temperature (row 2), DHM air temperature (row 3), PMD air temperature (row 4), WU air temperature (row 5), and CMA surface pressure (row 6). The study domain with dots showing ground-based stations for each evaluation source are shown in column 5. The plus signs and red lines in the box plots are shown as outliers and medians, respectively. A close-up sub-figure of the DHM stations is shown in column 6.

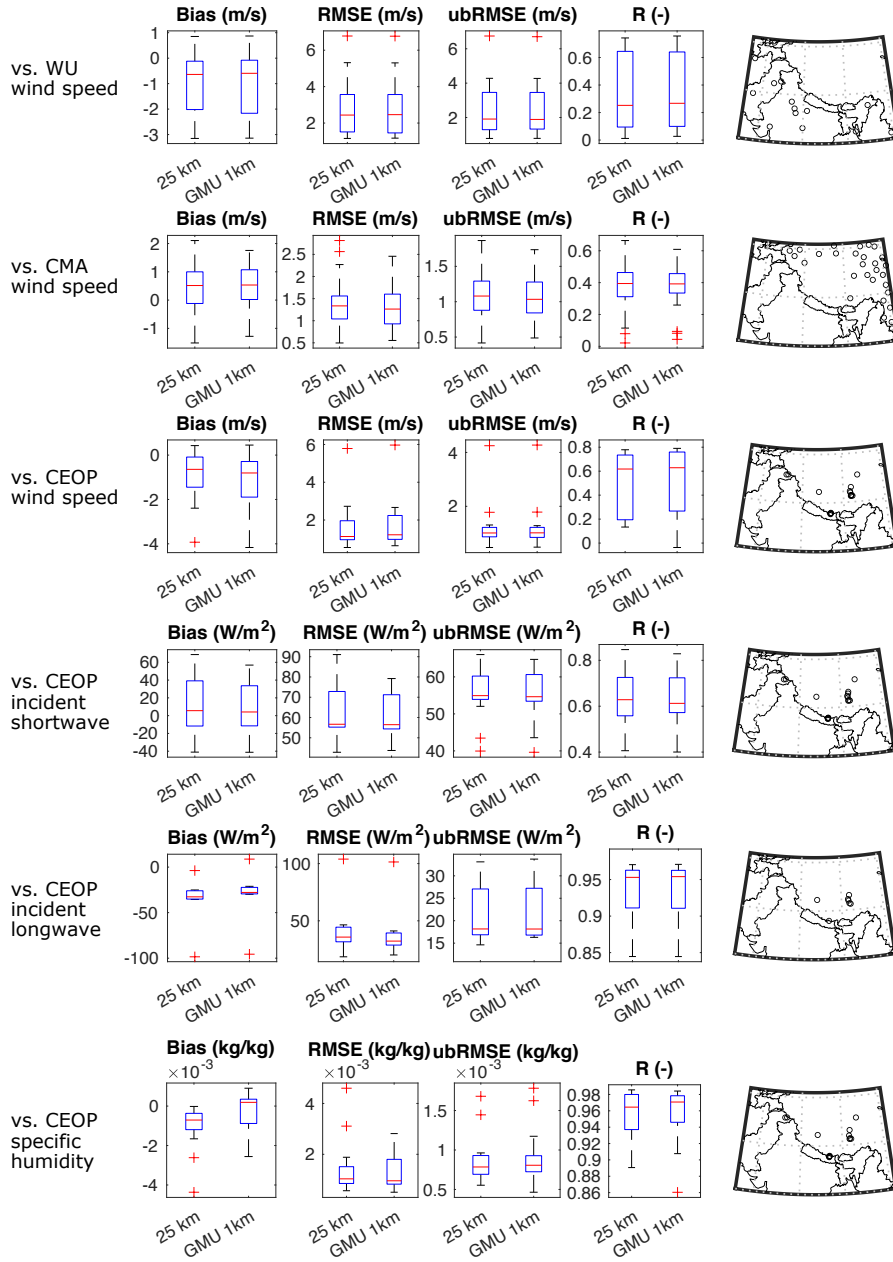


**Figure 4.** Same as Figure 3, but for the evaluation against ground-based WU wind speed (row 1), CMA wind speed (row 2), CEOP wind speed (row 3), CEOP incident shortwave radiation (row 4), CEOP incident longwave radiation (row 5), and CEOP specific humidity (row 6).

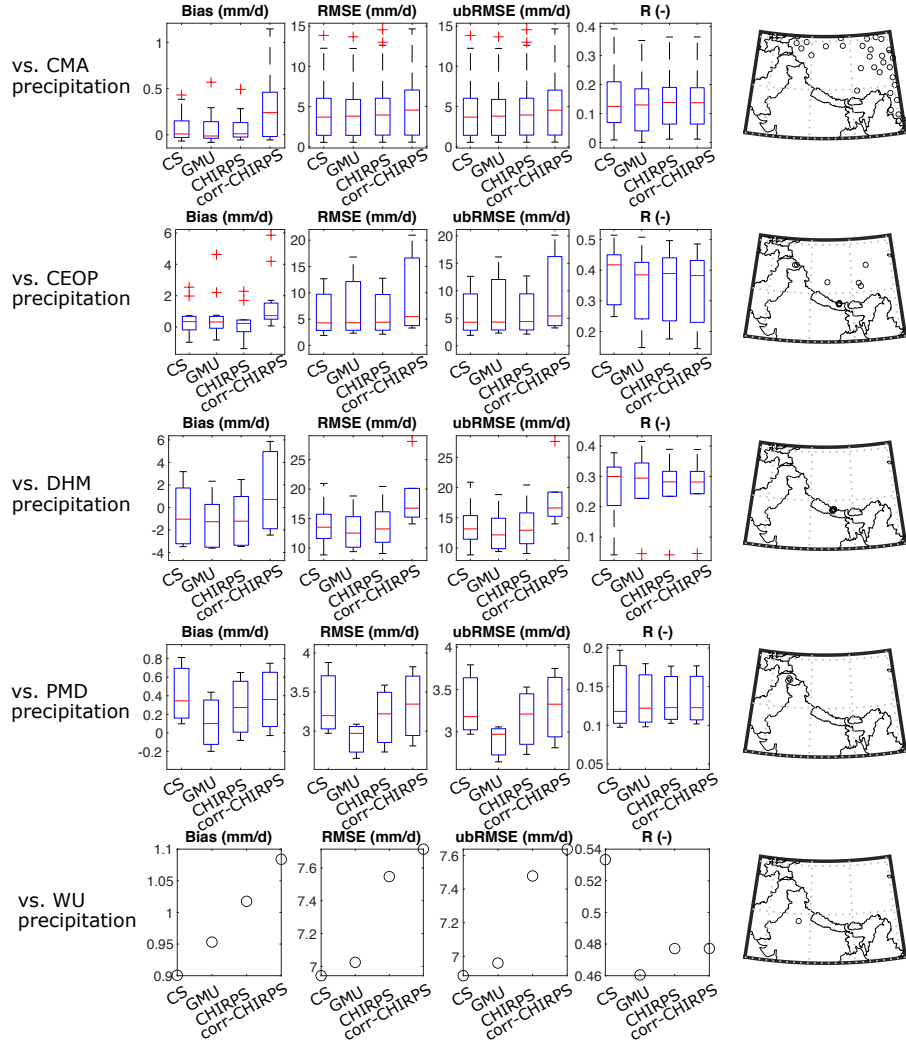


**Figure 5.** Box plots of bias (column 1), RMSE (column 2), ubRMSE (column 3), R (column 4) computed from HMA-Coarse, HMA-GMU, HMA-CHIRPS, and HMA-corr-CHIRPS in the evaluation against ground-based CMA daily precipitation (row 1), CEOP daily precipitation (row 2), DHM daily precipitation (row 3), PMD daily precipitation (row 4), and WU daily precipitation (row 5). The study domain with dots showing ground-based stations for each evaluation source are shown in column 5. The plus signs and red lines in the box plots are shown as outliers and medians, respectively. The prefix of the experimental name of “HMA” is omitted for clarity.

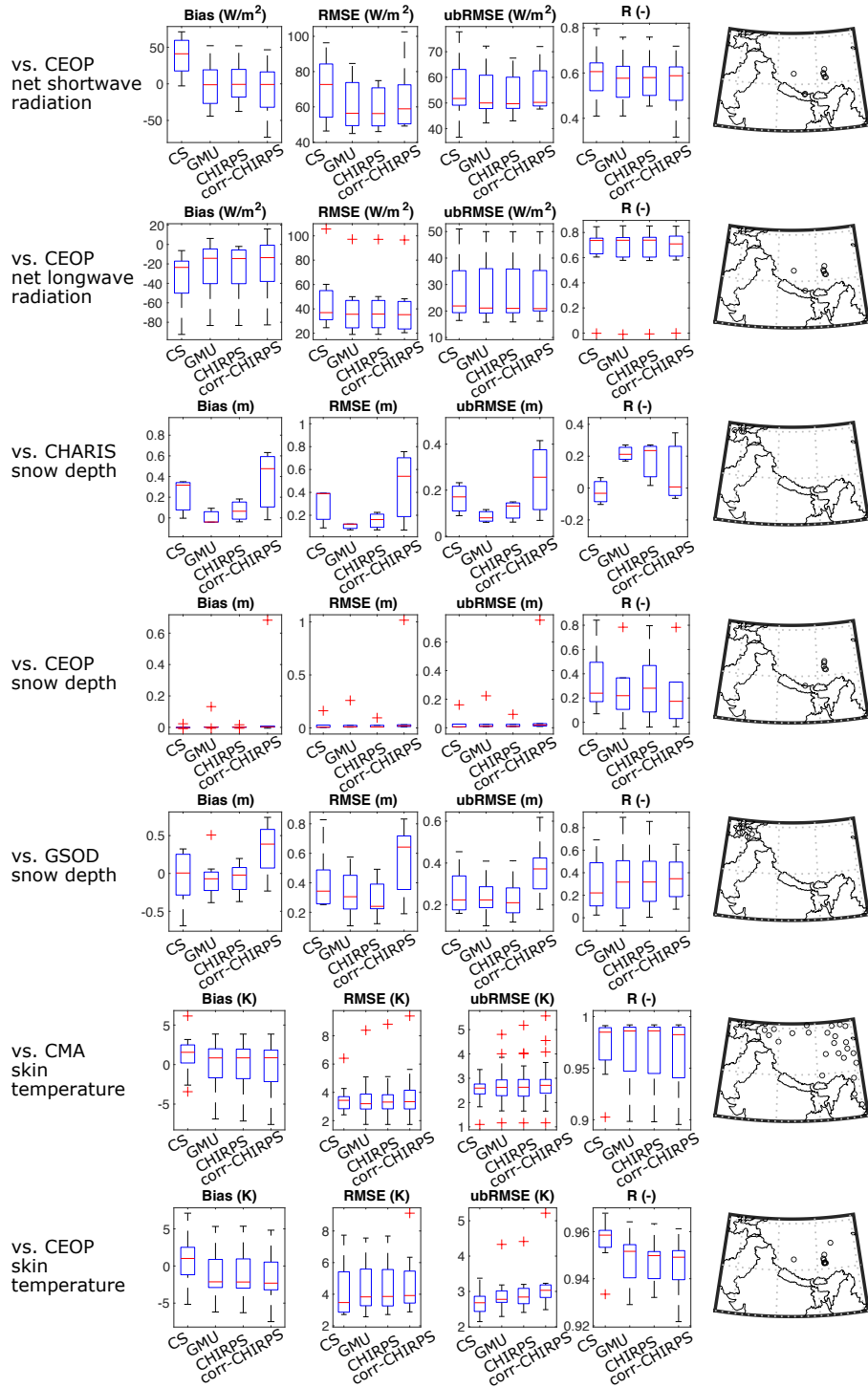


**Figure 6.** Same as Figure 5, but for the evaluation against ground-based CEOP net shortwave radiation (row 1), CEOP net longwave radiation (row 2), CHARIS snow depth (row 3), CEOP snow depth (row 4), GSOD snow depth (row 5), CMA skin temperature (row 6), and CEOP skin temperature (row 7).

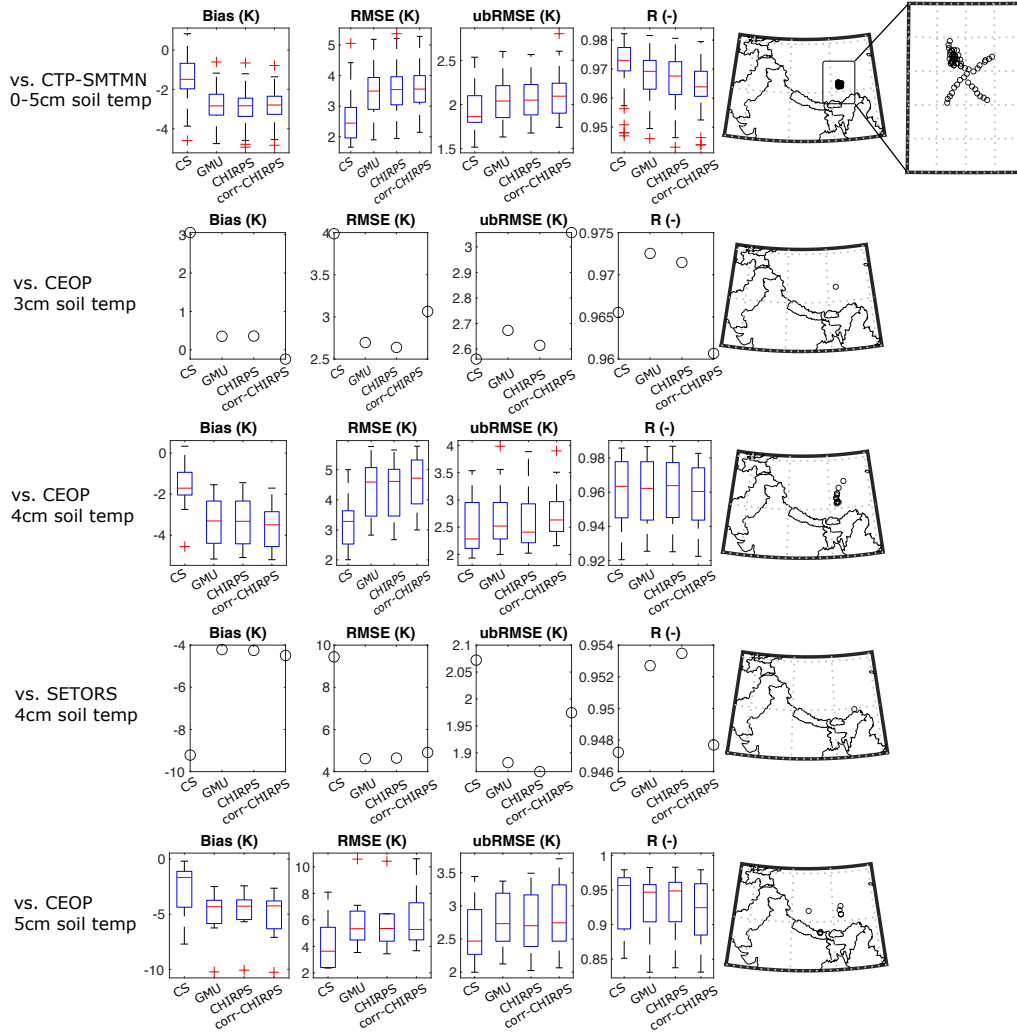


**Figure 7.** Same as Figure 5, but for the evaluation against ground-based CTP-SMTMN 0-5 cm soil temperature (row 1), CEOP 3 cm soil temperature (row 2), CEOP 4 cm soil temperature (row 3), SETORS 4 cm soil temperature (row 4), and CEOP 5 cm soil temperature (row 5). Note there is only one CEOP station measuring 3 cm soil temperature, and there is only one SETORS station. A close-up sub-figure of the CTP-SMTMN stations is shown in column 6.

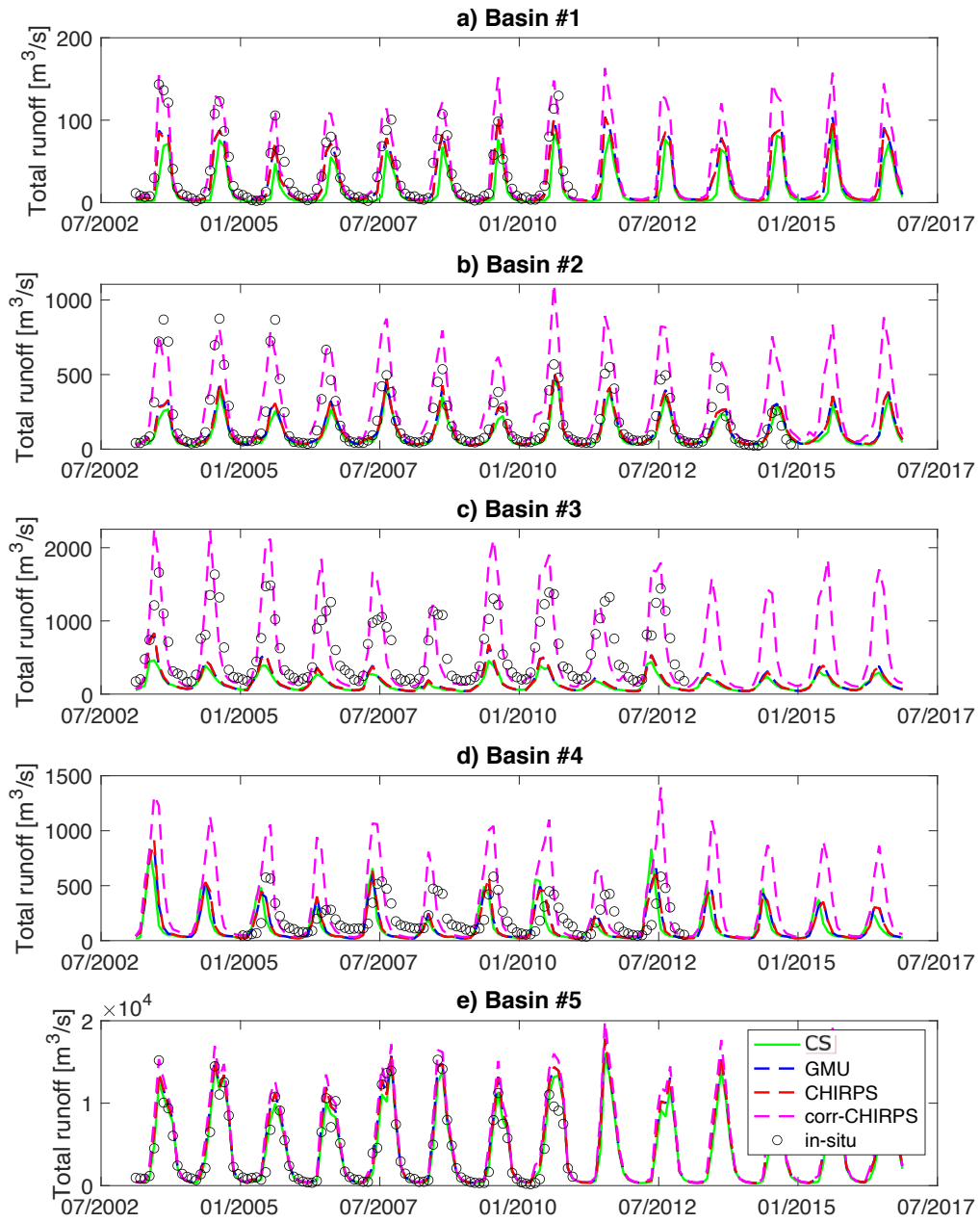


**Figure 8.** Monthly runoff estimates obtained from HMA-Coarse, HMA-GMU, HMA-CHIRPS, and HMA-corr-CHIRPS for the five gauged basins in the evaluation against ground-based measurements.

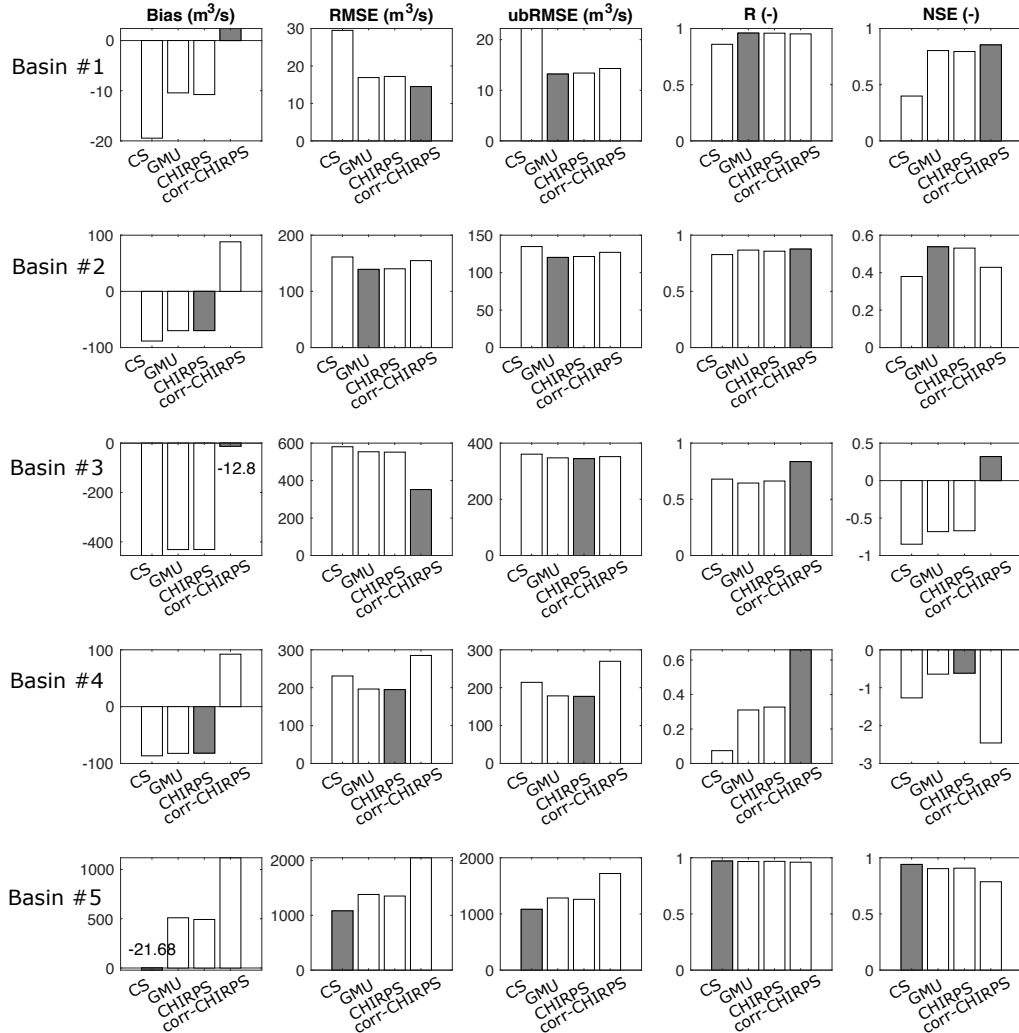


**Figure 9.** Statistics of bias (column 1), RMSE (column 2), ubRMSE (column 3), R (column 4), and NSE (column 5) computed from HMA-Coarse, HMA-GMU, HMA-CHIRPS, and HMA-corr-CHIRPS in the evaluation against five sets of ground-based monthly runoff measurements. Each row represents statistics for each basin. In addition, experiments with the best goodness-of-fit statistics for each basin are marked with grey bars or noted with numbers if their bars are too tiny to visualize.

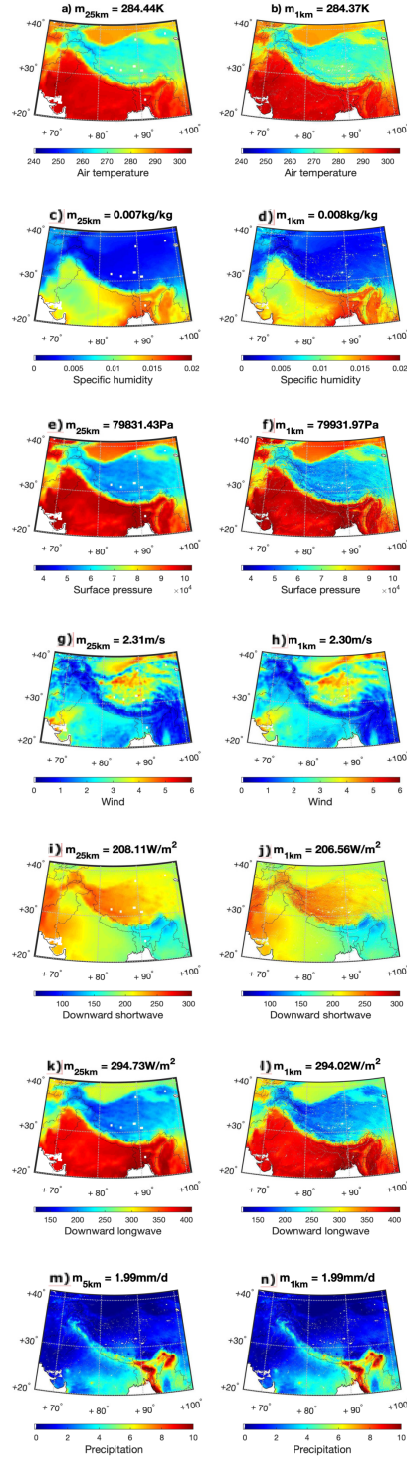


**Figure 10.** Multi-year (2003-2016) average of daily air temperature, specific humidity, surface pressure, wind speed, shortwave radiation, longwave radiation, and precipitation before and after being downscaled across HMA. m in the title denotes the domain-averaged value.

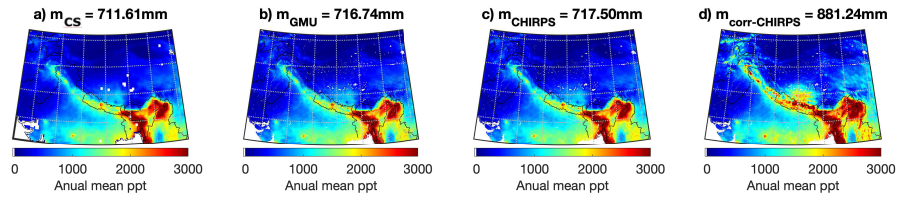


**Figure 11.** Annual mean total precipitation computed from a) HMA-Coarse, b) HMA-GMU, c) HMA-CHIRPS, and d) HMA-corr-CHIRPS.  $m$  in the title denotes the domain-averaged value.

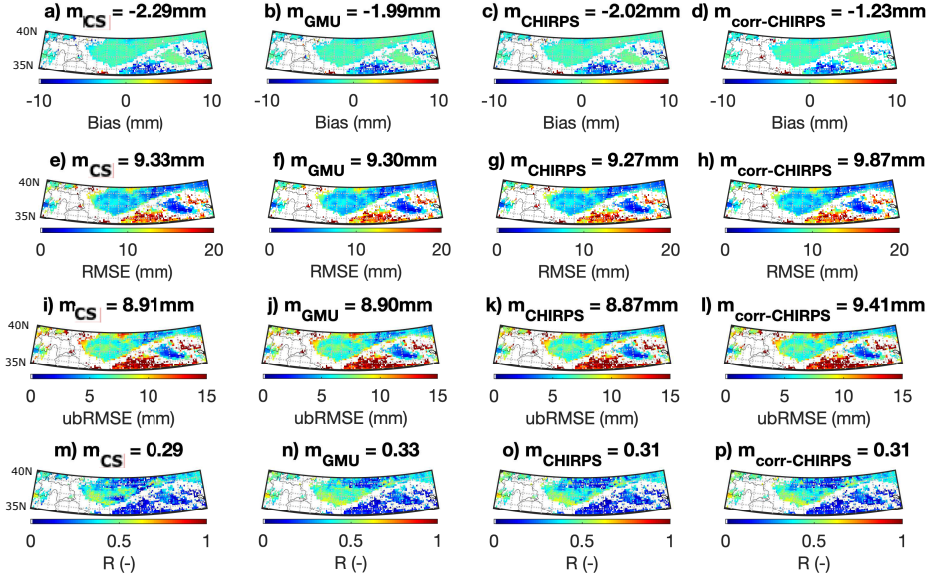


**Figure 12.** Goodness-of-fit statistics computed for HMA-Coarse (column 1), HMA-GMU (column 2), HMA-CHIRPS (column 3), and HMA-corr-CHIRPS (column 4) at a spatial resolution of  $0.25^\circ$  in the evaluation against the CGLS SWE product. Note the domain is truncated because the CGLS SWE product only covers area above latitude  $35^\circ\text{N}$ . Each row represents one set of goodness-of-fit statistics.  $m$  in the title denotes the domain-averaged value.

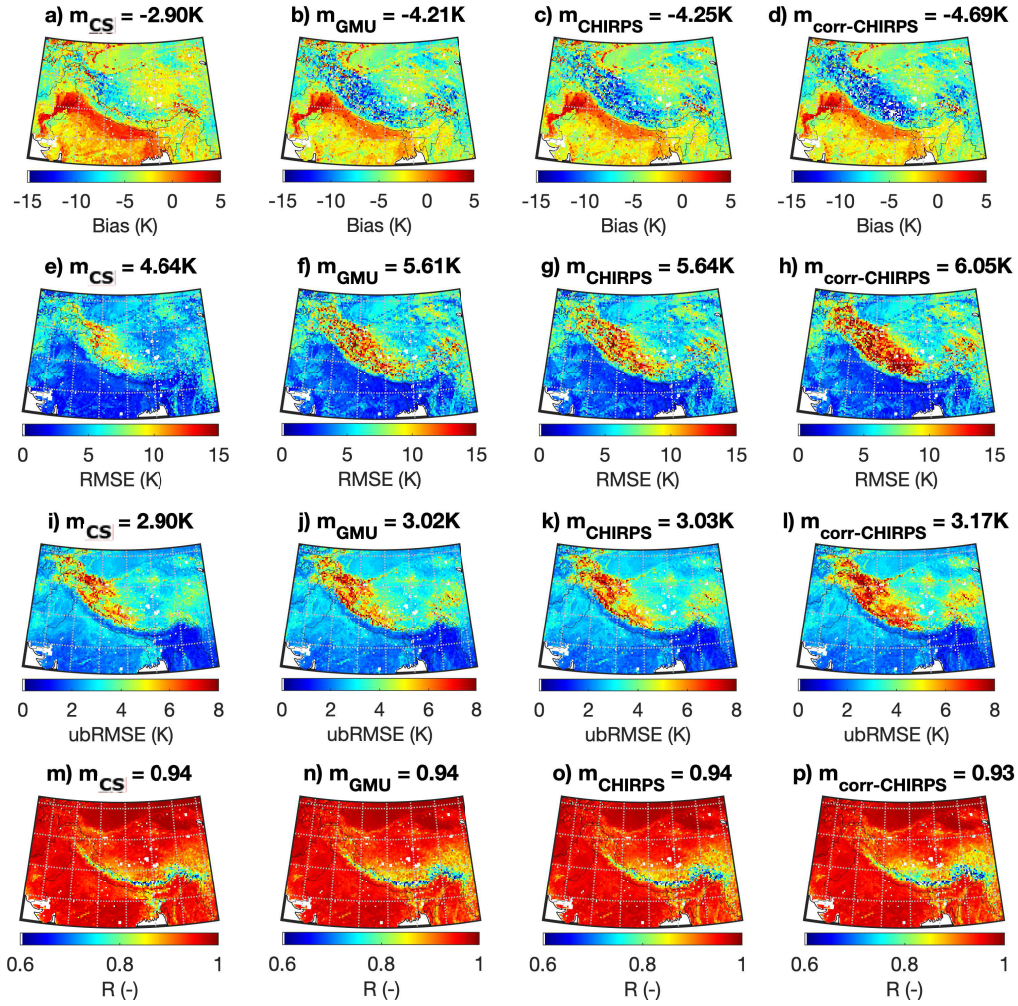


**Figure 13.** Goodness-of-fit statistics computed for HMA-Coarse (column 1), HMA-GMU (column 2), HMA-CHIRPS (column 3), and HMA-corr-CHIRPS (column 4) at a spatial resolution of  $0.25^\circ$  in the evaluation against the MODIS skin temperature product. Each row represents one set of goodness-of-fit statistics.  $m$  in the title denotes the domain-averaged value.

**Table 1.** Experiments used for evaluation.

Experiment name	Model output spatial resolution/temporal resolution	Precipitation input source (spatial resolution/temporal resolution)	Other meteorological forcings source (spatial resolution/temporal resolution)
HMA-Coarse (HMA-CS)	0.25°/daily	CHIRPS (0.05°/daily)	ECMWF (0.25°/6-hourly)
HMA-GMU	0.01°/daily	Downscaled CHIRPS (0.01°/6-hourly)	Downscaled ECMWF (0.01°/6-hourly)
HMA-CHIRPS	0.01°/daily	CHIRPS (0.05°/daily)	Downscaled ECMWF (0.01°/6-hourly)
HMA-corr-CHIRPS	0.01°/daily	Bias-corrected CHIRPS (0.05°/daily)	Downscaled ECMWF (0.01°/6-hourly)

**Table 2.** Summary of gauged basins shown in Figure 2. CHARIS = Contribution to High Asia Runoff from Ice and Snow project; DHM = Department of Hydrology and Meteorology in Nepal; GRDC = Global Runoff Data Centre.

Basin name (Figure number)	Drainage area (km <sup>2</sup> )	Data Source	Mean Elevation (m)
Basin #1 (Figure 2b)	654.9	DHM	1637.9
Basin #2 (Figure 2c)	4629.1	DHM	4329.1
Basin #3 (Figure 2d)	10320.6	CHARIS	3092.8
Basin #4 (Figure 2e)	29110.9	CHARIS	3534.2
Basin #5 (Figure 2f)	110350.0	GRDC	680.7

**Table 3.** Summary of meteorological forcings evaluation (except for precipitation; see precipitation evaluation in Table 4) in the comparisons against ground-based stations. Forcing fields from ECMWF before downscaling at  $0.25^\circ$  and after downscaling at  $0.01^\circ$  are evaluated. The final weighted scores are calculated following the method described in Section A and higher weighted scores are bold. CMA = Chinese Meteorological Administration; CEOP = Coordinated Enhanced Observing Period project; DHM = Department of Hydrology and Meteorology in Nepal; PMD = Pakistan Meteorology Department; WU = Weather Underground.

Data Source	Number of stations (Mean elevation)	Variables (temporal scale)	Weighted score by $0.25^\circ$	Weighted score by $0.01^\circ$
CMA	30 (2442.7m)	Air temperature (daily)	3.47	<b>3.76</b>
CEOP	16 (4263.5m)	Air temperature (daily)	3.49	<b>3.94</b>
DHM	6 (2689.7m)	Air temperature (daily)	<b>3.41</b>	3.04
PMD	3 (1360.7m)	Air temperature (daily)	2.83	<b>3.55</b>
WU	15 (393.9m)	Air temperature (daily)	3.56	<b>3.89</b>
CMA	30 (2442.7m)	Surface pressure (daily)	2.29	<b>4.00</b>
WU	14 (414.1m)	Wind speed (daily)	<b>3.97</b>	3.94
CMA	30 (2442.7m)	Wind speed (daily)	3.80	<b>3.86</b>
CEOP	18 (4264.4m)	Wind speed (daily)	<b>3.96</b>	3.71
CEOP	16 (4263.5m)	Incident shortwave (daily)	3.71	<b>3.93</b>
CEOP	7 (4684.8m)	Incident longwave (daily)	3.70	<b>3.98</b>
CEOP	14 (4181.2m)	Specific humidity (daily)	3.38	<b>3.65</b>
Total scores			41.57	<b>45.25</b>

**Table 4.** Summary of precipitation and model states evaluation in the comparisons against ground-based stations. Experiments listed in Table 1 are evaluated. The final weighted scores are calculated following the method described in Section A and higher weighted scores are bold. CHARIS = Contribution to High Asia Runoff from Ice and Snow project; CMA = Chinese Meteorological Administration; CTP-SMTMN = Central Tibetan Plateau Soil Moisture and Temperature Monitoring Network; CEOP = Coordinated Enhanced Observing Period project; GSOD = Global Summary of the Day; SETORS = Southeastern Tibet Observation and Research Station for the Alpine Environment.

Data Source	Number of stations (Mean elevation)	Variables (temporal scale)	Weighted score by HMA-Coarse	Weighted score by HMA-GMU	Weighted score by HMA-CHIRPS	Weighted score by HMA-corr-CHIRPS
CMA	30 (2442.7m)	Precipitation (daily)	3.75	3.79	<b>3.83</b>	2.91
CEOP	11 (4036.3m)	Precipitation (daily)	3.72	3.15	<b>3.85</b>	2.49
DHM	6 (2689.7m)	Precipitation (daily)	<b>3.59</b>	3.37	3.42	3.12
PMD	3 (1360.7m)	Precipitation (daily)	2.82	<b>3.94</b>	3.05	2.86
WU	1 (250.0m)	Precipitation (daily)	<b>4.00</b>	3.79	3.62	3.53
CEOP	8 (4578.3m)	Net shortwave (daily)	3.16	3.73	<b>3.77</b>	3.22
CEOP	7 (4684.8m)	Net longwave (daily)	3.69	3.74	3.74	<b>3.83</b>
CHARIS	3 (1937.7m)	Snow depth (daily)	1.16	<b>4.00</b>	2.13	0.86
CEOP	6 (4777.9m)	Snow depth (daily)	3.38	2.87	<b>3.50</b>	1.91
GSOD	8 (2303.3m)	Snow depth (daily)	3.01	3.61	<b>3.71</b>	2.46
CMA	24 (2315.6m)	Skin temp (daily)	<b>3.50</b>	2.87	3.32	2.69
CEOP	11 (4587.3m)	Skin temp (daily)	<b>3.74</b>	3.60	3.50	3.45
CTP-SMTMN	63 (4648.3m)	0-5cm soil temp (daily)	<b>3.79</b>	3.26	3.32	3.46
CEOP	1 (5038.6m)	3cm soil temp (daily)	2.73	3.63	3.66	<b>3.69</b>
CEOP	12 (4688.5m)	4cm soil temp (daily)	<b>3.79</b>	3.05	3.07	3.24
SETORS	1 (3326.0m)	4cm soil temp (daily)	2.84	<b>3.99</b>	3.98	3.82
CEOP	9 (4356.2m)	5cm soil temp (daily)	3.48	3.46	<b>3.53</b>	3.05
Total scores			56.15	<b>59.85</b>	59.00	50.59

**Table 5.** Summary of reference satellite-based products used for evaluation. MODIS = Moderate Resolution Imaging Spectroradiometer; CGLS = Copernicus Global Land Service.

Data Source	Temporal coverage	Variables (temporal scale)
MODIS	01 Feb 2003 - 30 Nov 2016	Skin temperature (daily)
CGLS	01 Jan 2006 - 30 Nov 2016	SWE (daily)

**Table 6.** The normalized mutual information (NMI) index computed between 25-km and 1-km multi-year (2003-2016) average of daily forcing estimates (except precipitation), as well as between 5-km and 1-km multi-year average of daily precipitation estimates as shown in Figure 10.

Forcing field	NMI (-)
Air temperature	0.89
Specific humidity	0.95
Surface pressure	0.89
Wind speed	0.96
Downward surface shortwave radiation	0.82
Downward surface longwave radiation	0.93
Precipitation	0.93

## 892 A A scoring system for point-scale evaluations

893 Many evaluation data sources provide more than one station to compare against  
 894 (see Tables 3 and 4). Therefore, the mean and the range (or spread) of the goodness-  
 895 of-fit statistics (including bias, RMSE, ubRMSE, and R) are computed as measures for  
 896 estimates accuracy and precision, respectively. The range of each set of goodness-of-fit  
 897 statistics is calculated as the difference between the third quartile and the first quartile  
 898 (a.k.a., interquartile range (IQR)). The lower the IQR is, the lower the spread is, and  
 899 the higher the precision is achieved by the corresponding experiment. However, if the  
 900 number of stations used for evaluation is less than three, the IQRs of goodness-of-fit statis-  
 901 tics are not calculated, and only the means of them are calculated. As a second step, for  
 902 each set of the goodness-of-fit statistics, we normalize the value (either mean or IQR of  
 903 the goodness-of-fit statistics) with respect to the best statistics obtained across all ex-  
 904 periments. Then, for each set of the model estimate, we sum up the normalized scores  
 905 across all four goodness-of-fit statistics for its accuracy (mean) and precision (IQR) mea-  
 906 sures, respectively. Third, we give equal weight (50% vs. 50%) to the accuracy and the  
 907 precision measures to derive the weighted score. Note that in the absence of the preci-  
 908 sion measure when the number of stations used for evaluation being less than three, we  
 909 give all weight (100%) to the accuracy measure. Finally, the experiment with the high-  
 910 est weighted score is deemed as the best model.

911 Using the CEOP air temperature evaluation as an example, through averaging the  
 912 bias computed via comparing against 16 ground-based stations, the mean bias of the air  
 913 temperature at  $0.25^\circ$  ( $0.01^\circ$ ) is  $-4.98$  K ( $-3.38$  K). Thus, the normalized score of the  $0.25^\circ$   
 914 ( $0.01^\circ$ ) air temperature estimates is 0.68 (1.00) in terms of mean bias. Similarly, the IQR  
 915 of bias of the air temperature at  $0.25^\circ$  ( $0.01^\circ$ ) is 4.04 K (3.46 K). Thus, the normalized  
 916 score of  $0.25^\circ$  ( $0.01^\circ$ ) air temperature estimates is 0.85 (1.00) in terms of the bias IQR.  
 917 Similar steps were also taken for other goodness-of-fit statistics. Then, the sum of the  
 918 normalized scores in the mean of the goodness-of-fit statistics for air temperature at  $0.25^\circ$   
 919 ( $0.01^\circ$ ) is 3.44 (3.99). The sum of the normalized scores in the IQRs of the goodness-  
 920 of-fit statistics for air temperature at  $0.25^\circ$  ( $0.01^\circ$ ) is 3.54 (3.89). Finally we give equal  
 921 weight (50% vs. 50%) to the accuracy and the precision measures. As a result, in the  
 922 evaluation against CEOP air temperature measurements, the weighted score for air tem-  
 923 perature at  $0.25^\circ$  ( $0.01^\circ$ ) is 3.49 (3.94). Since the downscaled air temperature yields a  
 924 higher weighted score than the original air temperature, we deem that the downscaled

925 air temperature performs better than the air temperature at the coarse spatial resolu-  
926 tion.

## Acknowledgments

This work was funded by NASA High Mountain Asia (NNH15ZDA001N-HMA) program, grant number NNX16AQ89G. We thank Shruti Mishra at the Argonne National Laboratory for providing runoff measurements at Basin #1 and Basin #2 obtained from the Department of Hydrology and Meteorology in Nepal. We thank Jing Tao at Lawrence Berkeley National Laboratory for sharing the codes related to shortwave downscaling. The CHIPRS precipitation data are available from <ftp://ftp.chg.ucsb.edu/pub/org/chg/products/>. The bias correction factors as applied to CHIRPS precipitation product is obtained from <http://www.gloh2o.org/pbcor/>. The CHARIS data were obtained from [http://himatmap.apps.nsidc.org/hma\\_insitu.html](http://himatmap.apps.nsidc.org/hma_insitu.html). The WU data were obtained from <https://www.wunderground.com>. The GRDC data were obtained from the Global Runoff Data Centre, 56068 Koblenz, Germany ([https://www.bafg.de/GRDC/EN/01\\_GRDC/grdc\\_node.html](https://www.bafg.de/GRDC/EN/01_GRDC/grdc_node.html)). The GSOD data were obtained from <https://data.noaa.gov/dataset/dataset/global-surface-summary-of-the-day-gsod>. The CMA data were obtained from [https://data.cma.cn/en/?r=data/detail&dataCode=SURF\\_CLI\\_CHN\\_MUL\\_DAY\\_CES\\_V3.0&keywords=daily](https://data.cma.cn/en/?r=data/detail&dataCode=SURF_CLI_CHN_MUL_DAY_CES_V3.0&keywords=daily). The CEOP data were obtained from [https://www.eol.ucar.edu/projects/ceop/dm/insitu/sites/ceop\\_ap/](https://www.eol.ucar.edu/projects/ceop/dm/insitu/sites/ceop_ap/). The CTP-SMTMN data were obtained from <http://dam.itpcas.ac.cn/rs/?q=data>, which was provided by Data Assimilation and Modeling Center for Tibetan Multi-spheres, Institute of Tibetan Plateau Research, Chinese Academy of Sciences. The SETORS data were obtained from <http://en.tpedatabase.cn/portal/MetaDataInfo.jsp?MetaDataId=197>. The SRTM elevation data may be downloaded from <http://srtm.csi.cgiar.org/srtmdata/>. All MODIS products were obtained from <https://earthdata.nasa.gov/>. The MEaSUREs landscape freeze/thaw product was obtained from <https://nsidc.org/data/nsidc-0728>. The CGLS SWE product (v1.0.2) was obtained from <https://land.copernicus.eu/global/products/swe>. We thank the entire NASA HiMAT team for sharing dataset and providing useful comments to the study. LIS models were run on ARGO, a research computing cluster provided by the Office of Research Computing at George Mason University, VA (<http://orc.gmu.edu>). The downscaling framework is implemented by functions/codes available via Mei's GitHub at <https://github.com/YiwenMei/AtmDS> and <https://github.com/YiwenMei/PrecipDS>. Downscaled products and model output generated in this study will be available at NASA Distributed Active Archive Center at National Snow and Ice Data Center.

960 **References**

- 961 Armstrong, R. L., Rittger, K., Brodzik, M. J., Racoviteanu, A., Barrett, A. P.,  
 962 Khalsa, S.-J. S., ... others (2019). Runoff from glacier ice and seasonal snow  
 963 in high asia: separating melt water sources in river flow. *Regional Environmen-*  
 964 *tal Change*, *19*(5), 1249–1261.
- 965 Beck, H. E., Wood, E. F., McVicar, T. R., Zambrano-Bigiarini, M., Alvarez-  
 966 Garretton, C., Baez-Villanueva, O. M., ... Karger, D. N. (2020). Bias cor-  
 967 rection of global high-resolution precipitation climatologies using streamflow  
 968 observations from 9372 catchments. *Journal of Climate*, *33*(4), 1299–1315.
- 969 Bohn, T. J., & Vivoni, E. R. (2019). Mod-lsp, modis-based parameters for hydro-  
 970 logic modeling of north american land cover change. *Scientific data*, *6*(1), 1–  
 971 13.
- 972 Bookhagen, B., & Burbank, D. W. (2010). Toward a complete himalayan hydro-  
 973 logical budget: Spatiotemporal distribution of snowmelt and rainfall and their  
 974 impact on river discharge. *Journal of Geophysical Research: Earth Surface*,  
 975 *115*(F3).
- 976 Buck, A. L. (1981). New equations for computing vapor pressure and enhancement  
 977 factor. *Journal of applied meteorology*, *20*(12), 1527–1532.
- 978 Cosgrove, B. A., Lohmann, D., Mitchell, K. E., Houser, P. R., Wood, E. F., Schaake,  
 979 J. C., ... others (2003). Real-time and retrospective forcing in the north  
 980 american land data assimilation system (nldas) project. *Journal of Geophysical*  
 981 *Research: Atmospheres*, *108*(D22).
- 982 Cover, T. M., & Thomas, J. A. (1991). Entropy, relative entropy and mutual infor-  
 983 mation. *Elements of information theory*, *2*, 1–55.
- 984 Dandekhya, S., England, M., Ghate, R., Goodrich, C., Nepal, S., Prakash, A., ...  
 985 Udas, P. (2017). The gandaki basin: Maintaining livelihoods in the face of  
 986 landslides, floods, and drought. *HI-AWARE Working Paper*, *9*.
- 987 Fiddes, J., & Gruber, S. (2014). Toposcale v. 1.0: downscaling gridded climate data  
 988 in complex terrain. *Geoscientific Model Development*, *7*(1), 387–405.
- 989 Funk, C., Peterson, P., Landsfeld, M., Pedreros, D., Verdin, J., Shukla, S., ... oth-  
 990 ers (2015). The climate hazards infrared precipitation with stationsa new  
 991 environmental record for monitoring extremes. *Scientific data*, *2*, 150066.
- 992 Gafurov, A., Vorogushyn, S., Farinotti, D., Duethmann, D., Merkushkin, A., &

- 993 Merz, B. (2015). Snow-cover reconstruction methodology for mountainous  
 994 regions based on historic in situ observations and recent remote sensing data.  
 995 *The Cryosphere*, 9(2), 451–463.
- 996 Ghatak, D., Zaitchik, B., Kumar, S., Matin, M., Bajracharya, B., Hain, C., & An-  
 997 derson, M. (2018). Influence of precipitation forcing uncertainty on hydro-  
 998 logical simulations with the nasa south asia land data assimilation system.  
 999 *Hydrology*, 5(4), 57.
- 1000 Grin, E., Schaller, M., & Ehlers, T. A. (2018). Spatial distribution of cosmogenic  
 1001 <sup>10</sup>be derived denudation rates between the western tian shan and northern  
 1002 pamir, tajikistan. *Geomorphology*, 321, 1–15.
- 1003 Gupta, A. S., & Tarboton, D. G. (2016). A tool for downscaling weather data from  
 1004 large-grid reanalysis products to finer spatial scales for distributed hydrological  
 1005 applications. *Environmental Modelling & Software*, 84, 50–69.
- 1006 Hannah, D. M., Kansakar, S. R., Gerrard, A., & Rees, G. (2005). Flow regimes of  
 1007 himalayan rivers of nepal: nature and spatial patterns. *Journal of Hydrology*,  
 1008 308(1-4), 18–32.
- 1009 Immerzeel, W. W., Droogers, P., De Jong, S., & Bierkens, M. (2009). Large-scale  
 1010 monitoring of snow cover and runoff simulation in himalayan river basins using  
 1011 remote sensing. *Remote sensing of Environment*, 113(1), 40–49.
- 1012 Kollet, S. J., Maxwell, R. M., Woodward, C. S., Smith, S., Vanderborght, J.,  
 1013 Vereecken, H., & Simmer, C. (2010). Proof of concept of regional scale hydro-  
 1014 logic simulations at hydrologic resolution utilizing massively parallel computer  
 1015 resources. *Water resources research*, 46(4).
- 1016 Konzelmann, T., van de Wal, R. S., Greuell, W., Bintanja, R., Henneken, E. A., &  
 1017 Abe-Ouchi, A. (1994). Parameterization of global and longwave incoming  
 1018 radiation for the greenland ice sheet. *Global and Planetary change*, 9(1-2),  
 1019 143–164.
- 1020 Kulmatov, R., Opp, C., Groll, M., & Kulmatova, D. (2013). Assessment of water  
 1021 quality of the trans-boundary zarafshan river in the territory of uzbekistan.  
 1022 *Journal of Water Resource and Protection*, 5(01), 17.
- 1023 Kumar, S. V., Peters-Lidard, C. D., Mocko, D., & Tian, Y. (2013). Multiscale  
 1024 evaluation of the improvements in surface snow simulation through terrain  
 1025 adjustments to radiation. *Journal of Hydrometeorology*, 14(1), 220–232.

- 1026 Kumar, S. V., Peters-Lidard, C. D., Tian, Y., Houser, P. R., Geiger, J., Olden, S.,  
 1027 ... others (2006). Land information system: An interoperable framework for  
 1028 high resolution land surface modeling. *Environmental modelling & software*,  
 1029 *21*(10), 1402–1415.
- 1030 Latt, Z. Z. (2015). *Flood assessment and improving flood forecasting for a monsoon*  
 1031 *dominated river basin: With emphasis on black-box models and gis* (Unpub-  
 1032 lished doctoral dissertation). Universitätsbibliothek der Leuphana Universität  
 1033 Lüneburg.
- 1034 Lawrence, M. G. (2005). The relationship between relative humidity and the dew-  
 1035 point temperature in moist air: A simple conversion and applications. *Bulletin*  
 1036 *of the American Meteorological Society*, *86*(2), 225–234.
- 1037 Marshall, J., & Plumb, R. A. (1989). *Atmosphere, ocean and climate dynamics: an*  
 1038 *introductory text* (Vol. 43). Academic Press.
- 1039 Mei, Y., Maggioni, V., Houser, P., Xue, Y., & Rouf, T. (2020). A nonparametric sta-  
 1040 tistical technique for spatial downscaling of precipitation over high mountain  
 1041 asia. *Water Resources Research (Accepted)*.
- 1042 Mishra, S. K., Hayse, J., Veselka, T., Yan, E., Kayastha, R. B., LaGory, K., ...  
 1043 Steiner, N. (2018). An integrated assessment approach for estimating the  
 1044 economic impacts of climate change on river systems: An application to hy-  
 1045 dropower and fisheries in a himalayan river, trishuli. *Environmental science &*  
 1046 *policy*, *87*, 102–111.
- 1047 Molteni, F., Buizza, R., Palmer, T. N., & Petroliagis, T. (1996). The ecmwf ensem-  
 1048 ble prediction system: Methodology and validation. *Quarterly journal of the*  
 1049 *royal meteorological society*, *122*(529), 73–119.
- 1050 Nash, J. E., & Sutcliffe, J. V. (1970). River flow forecasting through conceptual  
 1051 models part ia discussion of principles. *Journal of hydrology*, *10*(3), 282–290.
- 1052 Niu, G.-Y., Yang, Z.-L., Mitchell, K. E., Chen, F., Ek, M. B., Barlage, M., ... oth-  
 1053 ers (2011). The community noah land surface model with multiparameteriza-  
 1054 tion options (noah-mp): 1. model description and evaluation with local-scale  
 1055 measurements. *Journal of Geophysical Research: Atmospheres*, *116*(D12).
- 1056 Pulliainen, J. (2006). Mapping of snow water equivalent and snow depth in boreal  
 1057 and sub-arctic zones by assimilating space-borne microwave radiometer data  
 1058 and ground-based observations. *Remote Sensing of Environment*, *101*(2),

- 1059 257–269. doi: 10.1016/j.rse.2006.01.002
- 1060 Rouf, T., Mei, Y., Maggioni, V., Houser, P., & Noonan, M. (2019). A physically-  
1061 based atmospheric variables downscaling technique. *Journal of Hydrometeorol-*  
1062 *ogy*(2019).
- 1063 Ruiz-Arias, J., Alsamamra, H., Tovar-Pescador, J., & Pozo-Vázquez, D. (2010).  
1064 Proposal of a regressive model for the hourly diffuse solar radiation under all  
1065 sky conditions. *Energy Conversion and Management*, *51*(5), 881–893.
- 1066 Singh, R., Reager, J., Miller, N., & Famiglietti, J. (2015). Toward hyper-resolution  
1067 land-surface modeling: The effects of fine-scale topography and soil texture  
1068 on clm 4.0 simulations over the southwestern us. *Water Resources Research*,  
1069 *51*(4), 2648–2667.
- 1070 Strehl, A., & Ghosh, J. (2002). Cluster ensembles—a knowledge reuse framework for  
1071 combining multiple partitions. *Journal of machine learning research*, *3*(Dec),  
1072 583–617.
- 1073 Takala, M., Luoju, K., Pulliainen, J., Derksen, C., Lemmetyinen, J., Kärnä, J. P.,  
1074 ... Bojkov, B. (2011). Estimating northern hemisphere snow water equiva-  
1075 lent for climate research through assimilation of space-borne radiometer data  
1076 and ground-based measurements. *Remote Sensing of Environment*, *115*(12),  
1077 3517–3529. doi: 10.1016/j.rse.2011.08.014
- 1078 Tao, J., & Barros, A. P. (2018). Multi-year atmospheric forcing datasets for hydro-  
1079 logic modeling in regions of complex terrain—methodology and evaluation over  
1080 the integrated precipitation and hydrology experiment 2014 domain. *Journal*  
1081 *of hydrology*, *567*, 824–842.
- 1082 Wan, Z., Hook, S. J., & Hulley, G. C. (2015). Modis/terra land surface temper-  
1083 ature/emissivity daily 13 global 1km grid, version 6. *NASA EOSDIS LP*  
1084 *DAAC*.
- 1085 Xue, Y., Houser, P. R., Maggioni, V., Mei, Y., Kumar, S. V., & Yoon, Y. (2019).  
1086 Assimilation of satellite-based snow cover and freeze/thaw observations over  
1087 high mountain asia. *Frontiers in Earth Science*, *7*, 115. Retrieved from  
1088 <https://www.frontiersin.org/article/10.3389/feart.2019.00115> doi:  
1089 10.3389/feart.2019.00115
- 1090 Yang, K., Qin, J., Zhao, L., Chen, Y., Tang, W., Han, M., ... others (2013). A  
1091 multiscale soil moisture and freeze–thaw monitoring network on the third pole.

- 1092 *Bulletin of the American Meteorological Society*, 94(12), 1907–1916.
- 1093 Yang, Z.-L., Niu, G.-Y., Mitchell, K. E., Chen, F., Ek, M. B., Barlage, M., . . . oth-  
 1094 ers (2011). The community noah land surface model with multiparameteri-  
 1095 zation options (noah-mp): 2. evaluation over global river basins. *Journal of*  
 1096 *Geophysical Research: Atmospheres*, 116(D12).
- 1097 Yoon, Y., Kumar, S. V., Forman, B. A., Zaitchik, B., Kwon, Y., Qian, Y., . . . others  
 1098 (2019). Evaluating the uncertainty of terrestrial water budget components over  
 1099 high mountain asia. *Frontiers in Earth Science*, 7, 120.
- 1100 You, Q., Min, J., Zhang, W., Pepin, N., & Kang, S. (2015). Comparison of multiple  
 1101 datasets with gridded precipitation observations over the tibetan plateau. *Cli-*  
 1102 *mate Dynamics*, 45(3-4), 791–806.
- 1103 Yuan, F., Zhang, L., Win, K., Ren, L., Zhao, C., Zhu, Y., . . . Liu, Y. (2017). As-  
 1104 sessment of gpm and trmm multi-satellite precipitation products in streamflow  
 1105 simulations in a data-sparse mountainous watershed in myanmar. *Remote*  
 1106 *Sensing*, 9(3), 302.
- 1107 Zhang, C., Tang, Q., Chen, D., van der Ent, R. J., Liu, X., Li, W., & Haile, G. G.  
 1108 (2019). Moisture source changes contributed to different precipitation changes  
 1109 over the northern and southern tibetan plateau. *Journal of Hydrometeorology*,  
 1110 20(2), 217–229.
- 1111 Zhao, W., & Li, A. (2015). A review on land surface processes modelling over com-  
 1112 plex terrain. *Advances in Meteorology*, 2015.